


Sensitivity Analysis and Validation of a Computational Framework for Supersonic Parachute Inflation Dynamics

Faisal As'ad,^{*} Philip Avery,[†] and Charbel Farhat[‡]

Stanford University, Stanford, CA 94305

Jason Rabinovitch[§] 

Stevens Institute of Technology, Hoboken, NJ 07030

and

Marcus Lobbia[¶] and Navid Ataei^{**}

California Institute of Technology, Pasadena, CA 91109

<https://doi.org/10.2514/1.J064791>

The supersonic parachute inflation dynamics (PID) of the Advanced Supersonic Parachute Research (ASPIRE) SR03 parachute system, represented by a detailed computational model, are numerically simulated using a high-fidelity framework for fluid–structure interaction (FSI). Numerical results, in the form of representative quantities of interest, are validated against data from the ASPIRE SR03 flight test. The validation is performed on a predefined array of numerical simulations in order to investigate the robustness of these results and establish their sensitivities to identified critical modeling assumptions, including the resolution of the computational fluid dynamics mesh, the choice of the constitutive law for material modeling, and the choice of which physics to include. These sensitivities are evaluated with attention to their development and computational costs and to their associated uncertainties. The ultimate goal of the reported work is to pave the way for establishing best practices for the numerical simulation of supersonic PID and to advance the potential role of computational FSI in the design and evaluation processes of aerodynamic decelerator systems in general.

I. Introduction

CURRENTLY, supersonic parachutes remain the most effective and reliable decelerators for safely landing NASA's exploration rovers on Mars. Nonetheless, qualification of these parachutes prior to deployment is a nontrivial, costly, and time-intensive procedure, as it primarily involves system level wind-tunnel testing and atmospheric flight tests. Moreover, full-scale experiments do not always replicate mission conditions, and, even when they do, they give only empirical observations of parachute performance rather than a theoretical understanding of the underlying mechanisms that govern drag performance and potential material failure. Ergo, the parachute design and qualification process can benefit largely from the development of *validated* high-fidelity fluid–structure interaction (FSI) computational frameworks that can accurately simulate and predict supersonic parachute performance metrics, such as drag character, inflation time, suspension line load asymmetry and local stresses experienced by the canopy. Historically, most computational efforts in the literature have focused on the numerical simulation of the *post-inflation* regime [1–4], which is significantly easier to simulate,

or computational fluid dynamics (CFD) simulations over a static parachute [5]. However, experimental data suggest that peak loads are experienced during the inflation process [6]. Indeed, many canopy failures observed in flight tests conducted over the past four decades typically occurred during inflation [7,8]. Hence, understanding the complex dynamics involved during the *inflation* process in the supersonic regime is of paramount importance.

The numerical simulation of supersonic parachute inflation dynamics (PID) is a decidedly challenging task. It involves capturing heterogeneous flow features at different scales such as shocks, underexpanded jets, turbulent wakes, and thin boundary layers interacting with a highly nonlinear porous woven fabric canopy and thin braided suspension lines. Direct resolution of all the underlying physics is absolutely computationally intractable, and therefore it is necessary to either ignore some of physical phenomena or model them. This gives rise to model-form uncertainties or parametric uncertainties in these numerical simulations that can often hinder their reliability for real-world applications, such as qualification tests for parachute systems. Furthermore, different levels of approximations can result in massively different computational costs, and the involved accuracy–cost trade-off for the application of supersonic PID is not well-understood. More recently, there have been efforts in the literature to simulate the dynamics of the inflation regime [9–11]. Whilst the field has advanced significantly over the past decade in terms of modeling and computational capabilities, considerable effort in validation and uncertainty quantification is still required before numerical simulation techniques can aid or guide experimental parachute qualification.

As such, this paper aims to validate the AERO Suite multiphysics computational framework [12,13] in the numerical simulation of supersonic PID through numerical study. In doing so, it also aims to identify critical modeling choices and establish the sensitivities of the numerical simulation results to these choices. The validation effort focuses on the parachute system and flight conditions used in the Advanced Supersonic Parachute Inflation Research Experiment (ASPIRE) SR03 flight test, as performed in [11,14]; it draws on the abundance of experimental data available in [6,15,16].

The computation and modeling in this paper is based on a similar framework to that presented in [9], which focused on validation against experimental data from the 2012 landing of the Curiosity Mars rover. The authors have previously investigated validation and some

Presented as Paper 2024-4656 at the AIAA Aviation 2024 Forum, Las Vegas, NV, July 29–August 2, 2024; received 27 August 2024; revision received 21 October 2024; accepted for publication 25 October 2024; published online 17 December 2024. Copyright © 2024 by the authors. Published by the American Institute of Aeronautics and Astronautics, Inc., with permission. All requests for copying and permission to reprint should be submitted to CCC at www.copyright.com; employ the eISSN 1533-385X to initiate your request. See also AIAA Rights and Permissions www.aiaa.org/randp.

^{*}Ph.D. Candidate, Department of Aeronautics and Astronautics, Durand Building, Room 224; faisal3@stanford.edu.

[†]Senior Research Engineer, Department of Aeronautics and Astronautics, Durand Building, Room 214; pavery@stanford.edu.

[‡]Vivian Church Hoff Professor of Aircraft Structures, Department of Aeronautics and Astronautics and Institute for Computational and Mathematical Engineering, Durand Building, Room 257; cfarhat@stanford.edu. Fellow AIAA.

[§]Assistant Professor, Department of Mechanical Engineering, Edwin A. Stevens Hall 323; jrabinov@stevens.edu. Associate Fellow AIAA.

[¶]System Engineer, Entry, Descent, Landing & Advanced Technologies Group, Jet Propulsion Laboratory, 4800 Oak Grove Drive, M/S: 301-490; marcus.a.lobbia@jpl.nasa.gov.

^{**}Structural Engineer, Jet Propulsion Laboratory, 4800 Oak Grove Drive, M/S: M/S 321-130; navid.ataei@jpl.nasa.gov.

modeling sensitivities of this computational framework in the numerical simulation of the ASPIRE SR03 flight test in [14,17]. In light of lessons learned in these works, in addition to newly advanced computational capabilities, this paper revisits some of the previously studied modeling sensitivities and explores new ones, with higher fidelity numerical simulations. Explicitly, the validation effort aims to establish sensitivities of the numerical simulation results with respect to mesh resolution, nonlinearity in the canopy and/or suspension line material laws, the boundary conditions on the forebody, the law governing the dynamic adaptation of the fabric porosity, and the interaction of fluid with the suspension lines. The main goal of studying these modeling assumptions is to establish the value of using the higher fidelity options in relation to the additional computational cost they incur or the implementation effort required to enable them.

To this end, the remainder of the paper is organized as follows. Section II describes the details of the ASPIRE program and the SR03 flight test. Section III provides a brief summary of the AERO Suite computational framework and the relevant enabling numerical simulation technologies. Section IV describes in detail the computational models and assumptions used, discusses the different numerical simulation scenarios that are the subject of the validation effort, and presents numerical simulation results in the form of comparison against experimental data. Finally, Sec. V summarizes findings and concludes with lessons learned from the study.

II. Jet Propulsion Laboratory's ASPIRE Project and the SR03 Flight Test

The third and final flight test of JPL's ASPIRE program, SR03, took place on 7 September 2018 [6,18] (see Fig. 1). The purpose of the ASPIRE series of missions was to demonstrate the

high-speed deployment of parachute systems toward the development of a system that can be used to land payloads onto Mars. Specifically, it served as a qualification test for the parachute system of the Perseverance rover that landed on Mars on 18 February 2021.

Two different parachutes were evaluated during ASPIRE. The SR01 flight test carried a parachute almost identical to that used to land NASA's Mars Science Laboratory on Mars in 2012. The SR02 and SR03 carried parachutes of similar dimensions but reinforced with stronger materials and stitching to allow for withstanding of larger loads. Of the three tests, the SR03 test was deployed at the highest Mach number, was subject to the highest dynamic pressure, and achieved the highest peak load. Therefore, it is chosen in this paper as the focus for validation.

The supersonic disk-gap-band parachute system used for the SR03 flight test, including the canopy, suspension lines, riser line, and triple bridle lines, along with its slender forebody, is displayed in Fig. 2 in the as-fabricated configuration. The geometric parameters are reported in Table 1 and are obtained from [19]. The canopy consists of 80 disk gores and 80 band gores made of plain-woven custom-made Heathcoat fabric [20]. The leading and trailing edges of the disk and band are reinforced by circumferential stiffeners made of T-87130 Type VI Class 6a and Class 9 Kevlar webbing. The suspension line subsystem, made of 3200 lb Technora braided rope, consists of 40 lines that each originate from the upper end of the 10-ply 30,000 lb riser line, pass through the band and disk, cross at the center of the vent, pass through the disk and band again (on the opposite side), and finally return to the riser line attachment point. The six-ply 30,000 lb Kevlar webbing triple bridle lines attach to the upper end of the forebody at three points and meet at the lower end of the riser line. All aforementioned material specifications are reported on in [17].

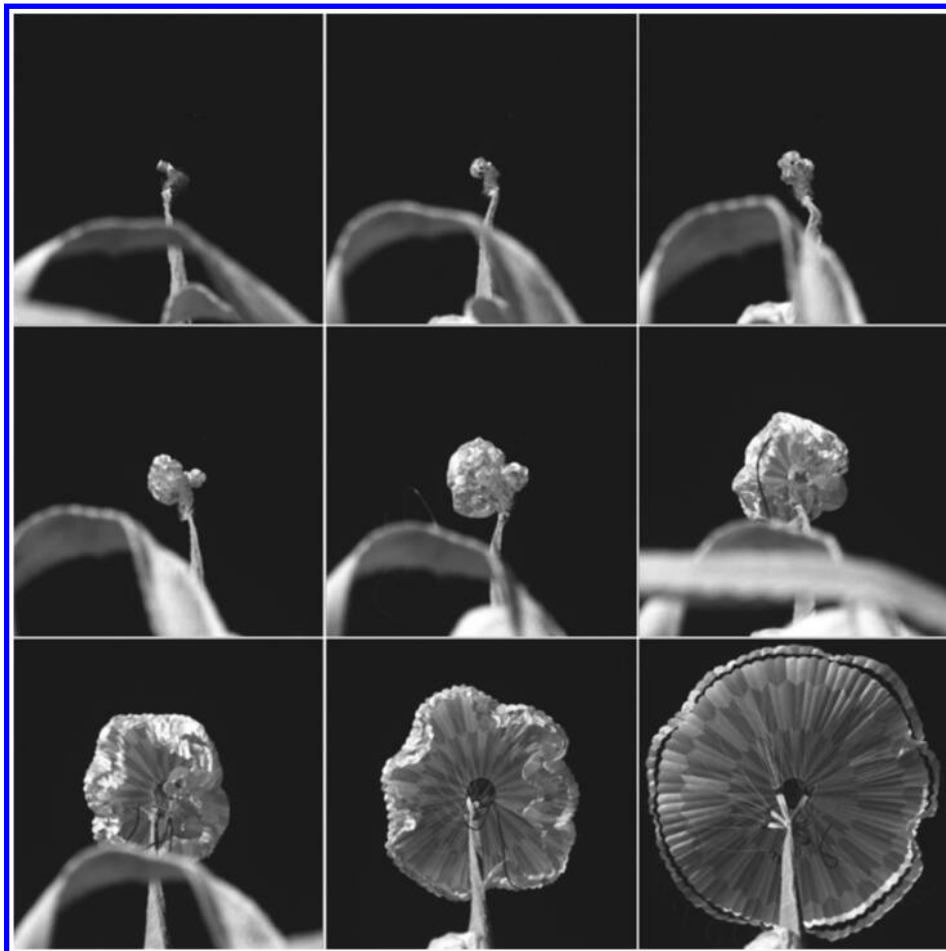


Fig. 1 Snapshots from the inflation of the ASPIRE SR03 parachute during flight test (images taken from the rear-facing camera attached to the back end of the ASPIRE forebody [18]).

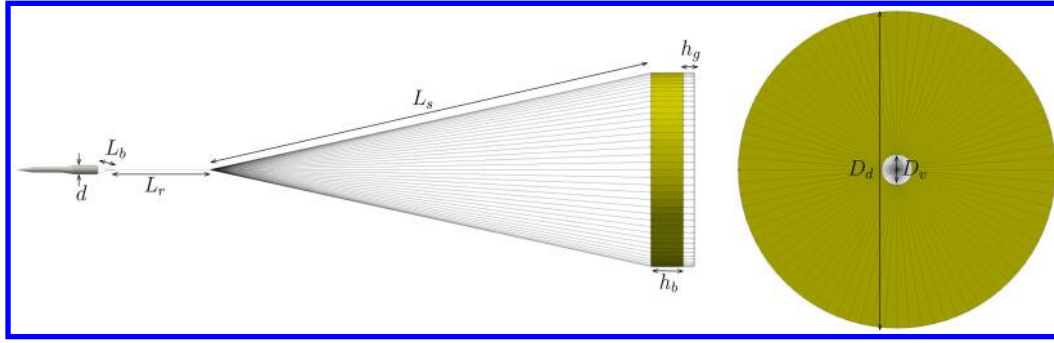


Fig. 2 ASPIRE SR03 parachute system in the as-fabricated configuration.

Table 1 Geometric parameters of the parachute used for the ASPIRE SR03 flight test [19]

Measurement	Symbol	Value, m
Suspension line length	L_s	36.53
Riser line length	L_r	7.7851
Bridle length	L_b	1.30
Disk diameter	D_d	15.652
Band height	h_b	2.6015
Gap height	h_g	0.903
Vent hole diameter	D_v	1.505
Forebody diameter	d	0.72

The parachute system was initially packed in a bag attached to the slender ASPIRE forebody on a sounding rocket. After being launched and separating from the first and second stages of the rocket stack, the 1277 kg payload, including the forebody and parachute system, reached apogee at an altitude of 51 km, before accelerating in a descent toward Earth. The mortar fire of the parachute occurred at a Mach number of 1.85. Shortly afterwards, the line-stretch phase of the parachute deployment was reached, which is when the tension in the suspension lines began to exhibit a measurable increase. Line-stretch was estimated to occur at a Mach number of 1.88, a wind-relative velocity of 584 m/s, a geodetic altitude of 37.7 km, and a flight path angle of -52.8° [6]. After the line-stretch phase, the parachute underwent a period of violent inflation until full inflation was reached. Then, it rapidly collapsed and reinflated, entering a regular cycle of partial collapse and reinflation, a phenomenon known as breathing [21]. During this process, it decelerated in a quasi-steady manner. These different phases of inflation are observable through the drag force generated in the SR03 flight test, as shown in Fig. 3. For this

paper, the flight phase of interest begins at the line-stretch phase and concludes 0.8 s later, which is deemed to be an appropriate window for capturing the essential features of the inflation dynamics.

III. Platform AERO Suite for the Numerical Simulation of Highly Nonlinear FSI Problems

The computational framework used for the numerical PID simulations is described in detail in [9,14] and implemented in the open-source integrated academic software AERO Suite, which comprises a compressible viscous flow solver, AERO-F; a nonlinear structural analyzer, AERO-S; and two auxiliary software modules—namely, a preprocessor for enabling the enforcement of transmission conditions in fluid–structure computations, MATCHER, and a pre/post-processor for massively parallel computations on distributed high-performance computing systems, SOWER. It has been validated on a large variety of highly nonlinear large-scale computations in the field of aerospace engineering [12,13]. AERO-F, AERO-S, and their coupling are briefly overviewed subsequently, with attention only to their capabilities that are most pertinent to PID: these are highlighted and referred to in Sec. IV.

A. Flow Solver AERO-F

AERO-F is a three-dimensional, domain-decomposition-based, compressible Euler/Navier–Stokes equation solver with turbulence modeling capabilities. It performs numerical flow simulations past still or moving, rigid or flexible, porous or nonporous obstacles. For turbulent flow computations, it offers Reynolds-averaged Navier–Stokes, static and dynamic large eddy simulation (LES), and variational multiscale LES, as well as detached eddy simulation methods, with or without a wall function. For flexible obstacles, it communicates with the structural analyzer AERO-S to perform high-fidelity aeroelastic and other types of FSI analyses.

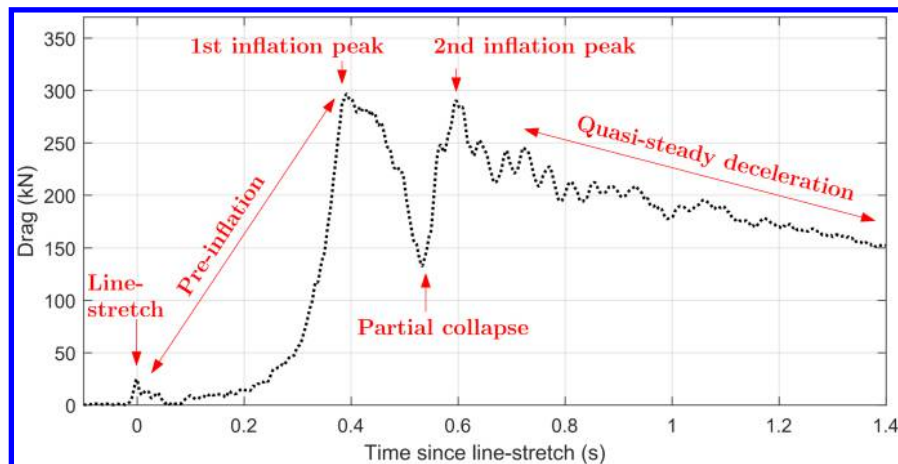


Fig. 3 Drag force generated during the ASPIRE SR03 flight test, with notable instances of the inflation labelled.

AERO-F operates on unstructured tetrahedral meshes. These can be body-fitted or non-body-fitted. In the latter case, discrete surfaces representing the obstacle are embedded in the fluid mesh and boundary conditions at the surface are enforced using an immersed boundary method—namely, the finite volume method with exact two-phase or two-material Riemann problems (FIVER) [22]. The CFD meshes and the embedded discrete surfaces can be static (fixed) or dynamic (moving and deforming). By default, AERO-F formulates and solves the governing fluid equations in the arbitrary Lagrangian Eulerian (ALE) framework if the CFD mesh is body-fitted and in the Eulerian framework if the CFD mesh is non-body-fitted. However, both frameworks can be combined to perform specific numerical simulations that benefit from both [23].

For spatial discretization, AERO-F blends the finite volume and finite element methods. Specifically, it performs the semidiscretization of the convective fluxes using a vertex-based finite volume method based on the Roe, HLLC, or HLLC upwind schemes or a rotated Riemann solver [24] that allows for different numerical fluxes to be used in orthogonal directions and that of the diffusive fluxes using a centered Galerkin approximation, achieving up to fifth-order spatial dissipation error and a sixth-order spatial dispersion error (and therefore fifth-order spatial accuracy). For temporal discretization, AERO-F offers several lower- and higher-order explicit and implicit time integrators that satisfy their respective discrete geometric conservation laws [25].

Finally, AERO-F is equipped with adaptive mesh refinement (AMR) [26] capabilities for both body-fitted and non-body-fitted CFD meshes. The mesh adaptation can be performed via either isotropic or anisotropic bisection, in the vicinity of both flow features and obstacles. When the mesh is refined or coarsened, AERO-F also leverages ParMETIS [27] to perform dynamic load balancing for managing memory resources and maximizing CPU efficiency across all used cores.

B. Nonlinear Structural Analyzer AERO-S

AERO-S is a finite element (FE) analyzer capable of linear and nonlinear structural, static, and dynamic analyses. It is also capable of detecting and resolving contact between surfaces using both a node-to-segment method and a mortar method, as well as crack propagation analysis. It is equipped with a comprehensive library of linear and nonlinear material models, which can be isotropic or anisotropic and elastic or inelastic. It uses a wide array of one-, two-, and three-dimensional FE elements, including beams, membranes, shells, and solids, with a combined corotational and Lagrangian formulation for handling geometric nonlinearities due to large rotations and large strains, in addition to lower- and higher-order time integrators.

C. Coupling of AERO-F and AERO-S

AERO-F and AERO-S are coupled using conservative algorithms for enforcing fluid–structure transmission conditions on matching or nonmatching fluid/structure interfaces, respectively (exchange of aerodynamic and structural data for multidisciplinary load computations and kinematic interface boundary conditions) and staggered solution procedures with provable accuracy and numerical stability properties for coupling multidisciplinary time integrators [28]. AERO-F and AERO-S, when coupled, can perform their respective analyses using different time step sizes, in which case one of them will subcycle in order to synchronize the timestamps and communicate information only when appropriate.

IV. Validation

The objective of this section is to primarily report on the validation of AERO Suite for supersonic PID problems through establishing sensitivities of numerical simulation results with respect to critical modeling assumptions. First, the computational model used to represent the ASPIRE SR03 problem introduced in Sec. II is described in detail. Subsequently, critical modeling assumptions that

give rise to an array of different numerical simulation scenarios are identified and discussed. Then, numerical simulation results are compared with experimental outcomes using representative quantities of interest (QoIs). Finally, the physical and numerical aspects of the results are discussed in the context of the modeling assumptions that led to the observed behaviors.

A. Detailed Finite Element Structural Model of the Parachute System

The FE model of the ASPIRE SR03 parachute used in the presented numerical simulations accounts for the canopy fabric, canopy circumferential stiffeners, suspension lines, riser line, triple bridle lines, and slender forebody. The undeformed or stress-free configuration of the model corresponds to the as-built geometry of the parachute, represented in Fig. 2. The canopy fabric is modeled using 267,878 three-node geometrically nonlinear triangular membrane elements with a single quadrature point, each assigned a specific material frame corresponding to the direction of the fabric warp fibers in the ASPIRE parachute. The membrane elements are compatible with nonlinear anisotropic material laws relating the Green–Lagrange strain to the second Piola–Kirchhoff stress. Specifically, two different material laws for woven fabric are considered: a linear orthotropic material law and a data-driven viscoelastic one represented by a mechanics-informed artificial neural network (ANN) [29,30]. The suspension lines, riser line, triple bridle lines, and circumferential stiffeners are modeled using a total of 80,000 two-node geometrically nonlinear Bernoulli beam elements. In one approach, the beam elements are assigned an infinitesimal linear elastic material law and their geometric nonlinearities are accounted for using a corotational formulation. Alternatively, the beam elements can be replaced with single-quadrature-point Lagrangian nonlinear bar elements and assigned a multiscale material law. The ASPIRE slender forebody is modeled using 4968 four-node rigid tetrahedral elements, which are assigned approximate densities to match the mass of the ASPIRE forebody. The rigidity constraint is enforced using a penalty method. The nominal mesh size of all membrane and beam elements is 5 cm [31], whereas that of the tetrahedral elements is 10 cm. The material properties assigned to the elements are described in detail in Table 2 and are obtained from multiples sources [6,17,32]. In total, the structural model has 827,834 degrees of freedom.

As an initial condition for the numerical FSI simulations, displacements are applied to the FE structural model to deform it into the accordion-like folding pattern shown in Fig. 4. This approach emulates the line-stretch condition while remaining compatible with the computationally feasible contact search method. The folding is executed so that the vent lines meet at an angle of 11 deg. Deforming the as-built configuration into the folded shape, rather than constructing the FE model in the folded shape, is advantageous. It allows the numerical FSI simulation to begin from a pre-stressed state, with suspension lines already under tension when the numerical simulation begins. The initial elongation of the suspension lines is calibrated so that the tension in the triple-bridle lines matches experimental load-pin measurements at line-stretch.

Because of the initial tight folding of the parachute, it is necessary to search for and resolve self-contact of the canopy to enforce nonpenetration of its elements. This is performed using the ACME library's node-to-segment approach [33]. In the first 0.4 s of the inflation, when the parachute packing is still tight, the contact search is performed globally. After the 0.4 s mark, when the parachute is close to full inflation, the contact search is massively accelerated by switching to an embarrassingly parallel local approach where contact needs be detected and enforced only between adjacent pairs of gores.

The FE system is integrated explicitly in time with a fixed time step size of 5×10^{-6} s, which was verified *a priori* to be conservatively below the maximum stability time step size allowed by the explicit central difference Newmark algorithm.

B. Embedded Discrete Surface Representation of the Parachute System

For the purpose of enabling the enforcement of the governing transmission conditions on fluid/structure interfaces, the wet surface

Table 2 Material properties adopted by the FE structural model [17] (the Young's moduli and Poisson's ratios are only relevant when a linear material law is applied)

Item	Primary Young's modulus, Pa	Secondary Young's modulus, Pa	Primary Poisson's ratio	Secondary Poisson's ratio	Density, $\text{kg} \cdot \text{m}^{-3}$	Thickness, m	Cross-sectional area, m^2
Canopy ^a	7.8×10^8	5.7×10^8	0.6	0.43	8.48×10^2	7.6×10^{-5}	—
Suspension line	1.82×10^{10}	—	0.4	0.4	4.84×10^2	—	2.02×10^{-5}
Riser line	1.86×10^{10}	—	0.4	0.4	7.51×10^2	—	1.79×10^{-3}
Bridle line	1.67×10^{10}	—	0.4	0.4	7.05×10^2	—	1.20×10^{-3}
Disk leading edge stiffener	1.35×10^{10}	—	0.4	0.4	4.54×10^2	—	2.69×10^{-5}
Disk trailing edge stiffener	1.09×10^{10}	—	0.4	0.4	5.25×10^2	—	6.45×10^{-5}
Band leading edge stiffener	1.35×10^{10}	—	0.4	0.4	4.54×10^2	—	2.69×10^{-5}
Band trailing edge stiffener	1.35×10^{10}	—	0.4	0.4	4.54×10^2	—	2.69×10^{-5}
Forebody nose-cone	—	—	—	—	1.0×10^4	—	—
Forebody remainder	—	—	—	—	4.58×10^2	—	—

^aProperties of the canopy fabric are measured from uniaxial tests of the ASPIRE Heathcoat material and obtained from private communication with Prof. Alireza Amirkhizi (see [32] for the testing methodology).

**Fig. 4** Initial configuration of the FE structural model prescribed for each performed numerical FSI simulation: a) zoomed-out side view, b) zoomed-in side view, and c) bottom view.

of the parachute system is represented by a discrete surface that is embedded in the CFD domain (and its mesh). The embedded discrete surface consists of 6,700,838 triangular elements split into three subsets: 6,369,133 elements of nominal size 1 mm forming enclosed cylinders representing the suspension lines (when relevant), 267,953 elements of nominal size 5 cm forming a two-sided representation of the canopy fabric, and 63,752 elements of nominal size 2 cm forming an enclosed body representing the ASPIRE forebody. The elements of this discretization are matched to those of the FE discretization using a parallel approach for matching fluid and structure meshes [34].

The portion of the embedded surface corresponding to the canopy is treated as a porous surface using the homogenized flux-body force treatment of compressible viscous porous wall boundary conditions described in [35]. The porosity values are approximated from imaging of F-111 Nylon (this study commenced before imaging and permeability measurements of the Heathcoat material were made available [36–38]). As such, a nominal porosity value of 8% is used and a square-shaped pore is assumed. On all other portions of the embedded surface, a no-slip boundary condition is imposed. To avoid the need to completely resolve the attached turbulent boundary layer on the slender forebody, Reichardt's nonlinear wall function [39] is used on the relevant portion of the embedded surface.

C. LES-Based CFD Model

The free-stream flow conditions for all the numerical simulations are taken to be those measured in the ASPIRE tests at line-stretch and are displayed in Table 3. The air is modeled as an ideal gas, the laminar viscosity is modeled using the Sutherland viscosity model, and the turbulence is modeled via an eddy-viscosity subgrid scale LES model [40]. The values of the various fluid mechanical properties are presented in Table 4.

Initially, the flow domain is discretized as a $160 \text{ m} \times 160 \text{ m} \times 220 \text{ m}$ rectangular prism consisting of 132,650 nodes and 750,000

Table 3 Free-stream flow conditions

Freestream parameter	Symbol	Value	Unit
Mach number	M_∞	1.88	—
Velocity	V_∞	585	m/s
Angle of attack	α_∞	0.9	°
Pressure	P_∞	414	Pa
Density	ρ_∞	6.01×10^{-3}	kg/m^3
Reynolds number (based on parachute diameter)	$Re_{D,\infty}$	3.3×10^6	—

Table 4 Fluid mechanical properties

Item	Symbol	Value
Sutherland reference temperature	T_0	110 K
Sutherland reference viscosity	μ_0	$1.46 \times 10^{-6} \text{ kg} \cdot \text{m}^{-1} \cdot \text{s}^{-1}$
Bulk viscosity	μ_v	0
Specific gas constant	R	$287.1 \text{ J kg}^{-1} \cdot \text{K}^{-1}$
Specific heat ratio	γ	1.4
Smagorinsky constant	C_s	0.2
Prandtl number	Pr	0.72

tetrahedral elements. At every 100 time steps, AMR [26] is used to isotropically refine and coarsen the mesh, based on the the flow features and the position of the embedded surface. The refinement and coarsening criteria for the flow features are based on the norm of the Hessian of the local velocity magnitude field; when it is above the refinement threshold, the mesh is refined locally, and when it is below the coarsening threshold, it is coarsened locally.

The velocity magnitude is chosen as the representative flow quantity as it allows for detecting both shocks and wakes, whereas the pressure, for example, would not be suitable as it does not vary significantly through a shear layer. The mesh is refined in the vicinity of the embedded surface using a criterion based on the minimum distance of the edge to the surface; edges that are closer than a specified distance to a surface are refined such that a smooth transition of the mesh sizes is obtained [26]. In the specific case of the embedded surface representing the suspension lines, the small radius of these representative cylinders makes their full resolution computationally intractable. Therefore, in the vicinity of these suspension lines, the distance-based criterion is used only as a coarse first level refinement of the nearby edges, and then edges are subsequently refined until no edge is intersected twice by the embedded surface, in order to obtain a minimally acceptable resolution [41]. The target edge length for the forebody wake refinement is chosen based on a mesh convergence study performed on the fixed-body numerical simulation of the flow around the forebody presented later in this subsection. The considered target edge lengths for the different AMR refinement criteria are specified in Table 5.

Away from the fluid–structure interfaces, the numerical fluxes are computed using the Harten–Lax–van Leer-contact (HLLC) Riemann solver and a second-order monotonic upstream-centered scheme for conservation laws with linear reconstruction, equipped with the Venkatakrishnan limiter [42]. At the fluid–structure interfaces, the numerical fluxes are constructed using the FIVER method [22]. The fluid system is integrated implicitly with a fixed time step size of 2×10^{-5} s using a diagonally implicit second-order Runge–Kutta (DIRK2) scheme. Accordingly, the structure system subcycles four times per fluid time step in order to synchronize the timestamps. However, when a negative pressure or density is encountered,

indicating nonlinear instability, the fluid time step size is halved and repeated until positivity is achieved, before it is ramped up back to its nominal value. The choice of nominal fluid time step size stems from the following convergence study.

Performing a proper convergence study on a full numerical FSI simulation of the ASPIRE SR03 inflation is computationally infeasible. Therefore, an alternative approach is taken here to perform mesh and time step size convergence studies for the numerical simulation of the flow around the ASPIRE forebody only. Because it has been often observed in the literature that the interaction between the forebody wake and the canopy bow shock plays a central role in the inflation regime [43–45], the main focus here is to obtain temporal and spatial fidelity that 1) triggers wake unsteadiness and 2) converges toward a nominal wake momentum deficit far downstream. To this end, target mesh sizes for the flow feature-based AMR are tested between 10 and 1 cm, and time step sizes are tested between 120 and 2 μ s.

Figure 5 plots the time histories of normalized velocity magnitude at two different downstream probe points, placed at 25 and 45 m downstream of the forebody, for the different temporal and spatial resolutions used, and Fig. 6 shows snapshots of the Mach contours from a few of the numerical simulations. As can be seen, the impact of refining the mesh from a size of 10 to 2 cm is nonmonotonic, indicating that the 10 and 5 cm mesh sizes still lie in the preasymptotic region of convergence. It should be noted that the unsteadiness in the wake is only observed at mesh sizes finer than 5 cm. Beyond this, the finer mesh sizes result in similar average momentum deficits downstream of the wake. Furthermore, the time step size does not seem to have a large influence on the character of the wake, at least when the second-order time-accurate DIRK2 scheme is adopted. However, Fig. 5 highlights the influence of the order of accuracy of the time integrator on the results, as it reveals that a lower-order time-integrator such as the first-order backward Euler (BE) scheme does not deliver the needed temporal accuracy at reasonable time step sizes.

From this, a minimum edge length of 2 cm and a time step size of 2×10^{-5} s are deemed sufficient to capture the desired flow features in the wake of the forebody. To maintain computational tractability during a numerical FSI simulation, a coarser minimum edge length can be used outside of the forebody wake region due to the bluff-body nature of the canopy flow and the lower resolution needed to resolve the shocks with sufficient sharpness.

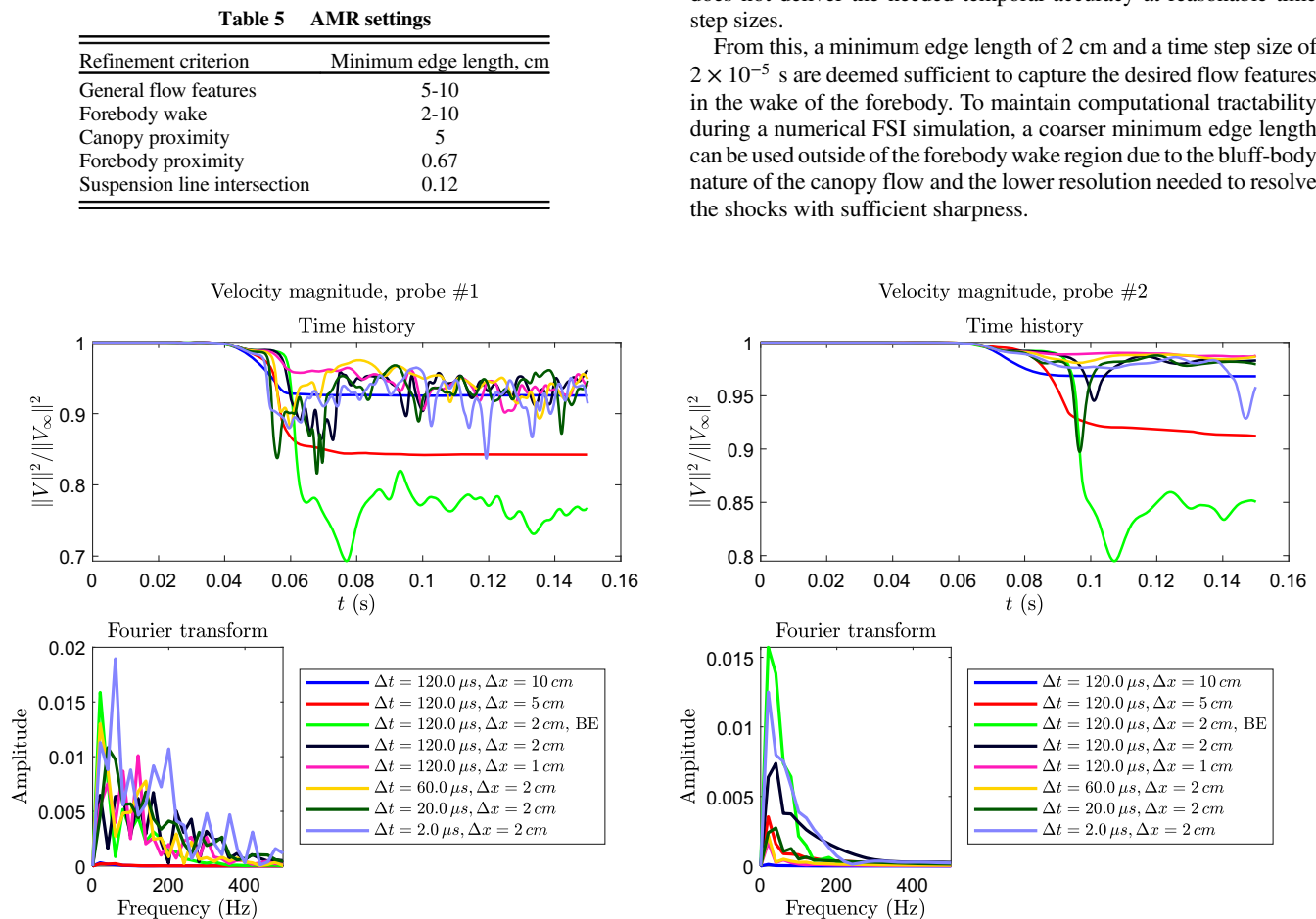


Fig. 5 Velocity magnitude of the flow over the static forebody at two downstream probes.

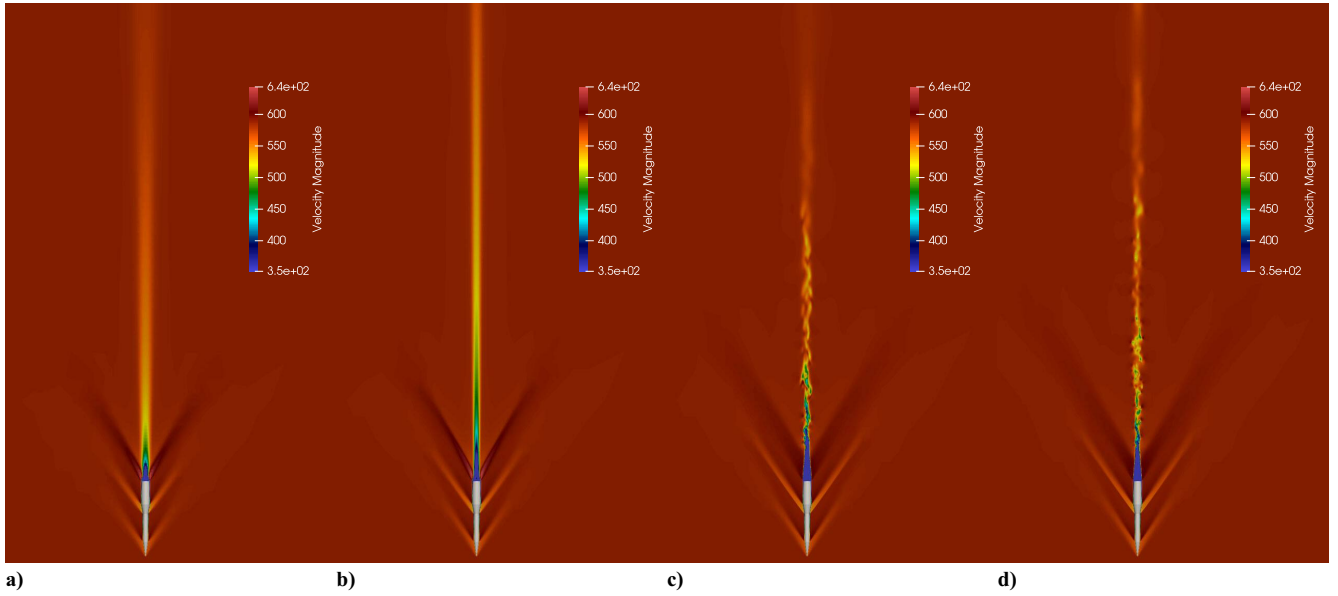


Fig. 6 Mach contours of the flow over the static forebody corresponding to different spatial and temporal resolutions: a) $\Delta t = 120 \mu s$ and $\Delta x = 10$ cm, b) $\Delta t = 120 \mu s$ and $\Delta x = 5$ cm, c) $\Delta t = 120 \mu s$ and $\Delta x = 2$ cm, and d) $\Delta t = 2 \mu s$ and $\Delta x = 2$ cm.

D. Numerical Simulation Scenarios

The computational cost of numerical supersonic PID simulations, the implementation effort required to enable them, and the amount of uncertainty in the models are all heavily influenced by the modeling and simulation choices made. These choices can include, but are not limited to, the mesh resolution, the constitutive models, and the choice of physics to be captured. Consequently, this paper aims to investigate the impact of identified critical modeling assumptions on the abilities of the numerical simulations to reproduce experimental results. The ultimate aim is to establish when expensive, uncertain, or implementation-intensive numerical simulation options can be avoided without a deterioration in predictive capability. To this end, the following modeling assumptions and parameters are considered:

1) *CFD mesh resolution: coarser vs finer.* Here, the coarser CFD mesh is defined by having a target mesh size of 10 cm around all flow features, whereas the finer CFD mesh has a target mesh size of 2 cm in the wake of the forebody and 5 cm near all other flow features. In both cases, the mesh size in the vicinity of the embedded surface is the same as outlined in Table 5. Although it was shown in Sec. IV.C that the finer mesh resolution is required to capture certain flow features such as an unsteady wake, it is not obvious whether those features will have a significant influence on integrated QoIs such as the drag. The use of the refined AMR mesh sizes has been observed to increase the number of degrees of freedom in the mesh by roughly a factor of 6, and thus it is desirable to use the coarser mesh size when it does not hinder accuracy.

2) *Forebody dynamics: fixed vs free.* In reality, the forebody of the parachute system is free to translate and rotate freely in response to loads acting on it. Most notably, it decelerates due to the parachute drag, which can impact inflation dynamics in two ways. First, the inertial deceleration effect can relieve the tension in the suspension lines and accordingly influence the opening of the canopy. Second, the deceleration dynamically reduces the effective free-stream velocity and therefore free-stream dynamic pressure, seen by the canopy, which is expected to have a significant effect on the long-term drag predicted (more precisely, the drag observed after the second inflation peak). Indeed, during roughly the first second of the inflation in the SR03 flight test, the forebody decelerates from a Mach number of 1.88 to a Mach number of 1.4. Whilst this behavior can be simulated with a pure embedded boundary method, it runs the risk of the parachute system getting undesirably close to the boundary of the CFD domain or alternatively necessitates the use of an excessively large computational fluid domain.

Furthermore, because there would be significant bulk translation of the entire parachute system through the CFD mesh, it would require a large number of refinement and coarsening actions performed by AMR, which can invoke an intractable computational cost and pollute the solution accuracy. Therefore, pure embedded boundary methods are practically limited to modeling the forebody dynamics by fixing it in space (equivalently, assigning it infinite mass). On the other hand, using an embedded-ALE hybrid framework [23], in which the CFD mesh is deformed rigidly according to the rigid body modes of the forebody, allows for the forebody to remain in a fixed position with respect to the CFD mesh, thus circumventing the aforementioned issues. Although the use of the embedded-ALE framework does not invoke any tangible additional computational cost, it requires a substantial implementation effort and thus is not available in many CFD codes.

3) *Canopy material law: linear single-scale vs nonlinear multiscale.* The choice of a canopy material law is expected to influence the dynamic response of the canopy and the predicted stresses. Although the tangent modulus in a linear material law can be fitted to any available experimental data, a linear law cannot capture typical fabric characteristics such as weakness in compression, stiffening in tension, strain-rate dependence, and dissipation. Furthermore, experimental data tend to be limited, and thus they would likely not capture the coupled biaxial and axial-shear relationships. Conversely, a nonlinear material law, in the form of a mechanics-informed viscoelastic ANN based on a woven fabric multiscale model as detailed in [29], can capture the time dependency and the nonlinearities associated with complex strain states, while still remaining mechanically consistent and thermodynamically stable. Nonetheless, this requires the training of the ANN-based model and the implementation effort involved in formulating it. Furthermore, it adds computational cost incurred from the execution of the ANN-based constitutive law at each structural time step for all canopy elements. As such, the worth of its inclusion should be investigated.

4) *Suspension lines and stiffeners material laws: linear single-scale vs multiscale.* The material law governing the suspension lines and circumferential stiffeners can also have a significant impact on the inflation character. Bernoulli beam elements compute their bending rigidity based on the geometric cross-sectional moment of inertia assuming a homogeneous (metallic) material and behave similarly in compression and tension. However, the soft Technora braided ropes that constitute the suspension lines have a significantly lower bending rigidity than their geometrically equivalent homogeneous

counterparts and exhibit weakness in compression. Therefore, a materially nonlinear beam element is required to capture their behavior. However, in lieu of a nonlinear beam implementation, this behavior is mimicked with a nonlinear bar element, equipped with the following proposed nonlinear heuristic material law representing the axial behavior:

$$S_{11} = A \left[\ln \left((e^C - 1) e^{BE_{11}} + 1 \right) - C \right]$$

where S_{11} and E_{11} are the axial components of the second Piola–Kirchhoff stress tensor and the Green–Lagrange strain tensor, respectively, and the tunable parameters A , B , and C are calibrated from data obtained by homogenizing a braided rope multiscale model. In the absence of sufficient validation data, the multiscale model itself is calibrated such that the load at the reported maximum elongation matches its experimental counterpart reported in [17]. Importantly, the heuristic model, by construction, exhibits weakness in compression and stiffens in tension. The use of bar elements rather than beam elements, despite their lack of bending stiffness, is justified due to the extremely low bending stiffness of soft braided ropes. Ultimately, capturing these characteristic behaviors is important as overpredicting the bending and compressive stiffnesses can lead to nonphysical phenomena and excess mechanical energy stored in the parachute system.

4) *FSI at the suspension lines: accounted for (two-way coupled) vs unaccounted for (uncoupled)*. The interaction of the dynamics of the suspension lines with the supersonic viscous flow can dictate the upstream flow conditions seen by the canopy. Previous numerical results [14] suggest that such an interaction can noticeably change the shape of the bow shock near the canopy and consequently influence its partial collapse. The significance of this FSI is also supported by the literature [46]. In the computational framework discussed in this paper, this interaction can be accounted for not only by modeling the structural dynamics of the suspension lines using bar or beam elements, but, equally importantly, also by representing the geometry of these lines by thin cylinders and embedding discrete approximations of their surfaces in the CFD fluid mesh. This allows the dynamic (deformable) geometry of each suspension line to influence the flow and enables the transfer to the aforementioned bar or beam elements of the appropriate aerodynamic loads experienced by the suspension lines [41]. Alternatively, the FSI at the suspension lines can be ignored, simply by not embedding in the CFD mesh any discrete representation of the surface geometry of any line (although the suspension lines are still included in the structural model). Whilst the former modeling decision leads to a higher fidelity computational model, it incurs a significant additional computational burden as 1) it requires a higher CFD mesh resolution in the vicinity of the suspension lines, 2) it requires computing mesh intersections and aerodynamic loads on more than 3 million additional embedded surface elements, and 3) it requires using a smaller time step size, even when the fluid subsystem is advanced in time using an implicit time integrator.

6) *Porosity modeling: constant vs stretch-dependent*. The porosity of the canopy fabric plays an important role in both a parachute's stability and its ability to generate drag. Larger porosity values stabilize the parachute but lead to a decrease in drag [47]. As seen in [36], the porosity of a parachute canopy fabric can change drastically as a function of the strain state. Therefore, this means the porosity of an element of the embedded surface representing the canopy should ideally be allowed to locally change through time. It is possible that capturing this phenomenon can aid in correctly predicting the large generated parachute loads, which tends to occur when the canopy is under maximal strain and thus the porosity is at its highest. Therefore, the two approaches investigated here are to use a constant value for the porosity corresponding to the strain-free measurement or to adapt it throughout the numerical simulation using a predetermined strain-dependent law. In the absence of experimental data for the fabric's porosity as a function of strain, a heuristic law is implemented, namely, Payne's law [48], which gives a geometric relationship between the axial strains and the porosity. In this work, for the sake of simplicity, a symmetric

variation of Payne's law is used in tension, in which it is assumed that the strains in both directions are equal. Explicitly, the porosity at time t_n of element i of the canopy embedded surface, denoted by ζ_i^n , is given as

$$\zeta_i^n = \begin{cases} \frac{A_i^0}{A_i^n} \left(\sqrt{\frac{A_i^n}{A_i^0}} - \left(1 - \sqrt{\zeta_i^0} \right) \left(1 - \nu \left(\sqrt{\frac{A_i^n}{A_i^0}} - 1 \right) \right) \right)^2 & A_i^n \geq A_i^0 \\ (1 - \epsilon) \zeta_i^0 \exp \left(\beta_i \left(\frac{A_i^n}{A_i^0} - 1 \right) \right) + \epsilon \zeta_i^0 & A_i^n < A_i^0 \end{cases} \quad (1)$$

where $\beta_i = (\sqrt{\zeta_i^0} - \zeta_i^0)(\nu + 1)/(1 - \epsilon)\zeta_i^0$, A_i^n is the area of element i at time t_n , ν is Poisson's ratio, and $\epsilon \in [0, 1]$ is a user-defined factor. This mimics Payne's law in tension but performs a smooth transition to a value of $\epsilon\zeta_i^0$ in the limit of compression, in the absence of a better model for porosity in compression. In this work, a value of $\epsilon = 0.8$ is chosen arbitrarily, and $\nu = 0.51$ is used, corresponding to the average of the primary and secondary Poisson's ratios of the Heathcoat fabric. A more detailed analysis of the modeling of fabric porosity for the ASPIRE SR03 parachute material is provided in [37].

The aforementioned modeling assumptions and parameters are summarized in Table 6. The employed strategy for covering this parameter space is highlighted in Fig. 7. The result is a set of eight numerical simulation scenarios, with increasing fidelity moving from left to right. The baseline, numerical simulation (1), contains the lowest fidelity option for each modeling assumption and/or parameter, whereas numerical simulation (8) contains all of the higher fidelity options.

E. Numerical Results

For the purposes of validation, the results are presented in the form of comparisons to available experimental time histories of QoIs. The four chosen QoIs are the free-stream dynamic pressure, drag, canopy projected area, and canopy skirt shape. Snapshots of the parachute FE model and the Mach number fields are also presented to provide physical insights to the observed results. Unless otherwise stated, in each figure representing a time history, the experimental data are shifted in time so that the numerical simulation and experimental peak loads align, due to the arbitrary and artificial nature of the initial condition in the numerical FSI simulations.

All of the presented numerical simulations are performed on 2016 cores of AMD EPYC 7742 Rome CPUs on NASA's Aitken cluster: 1920 cores dedicated to the fluid solver and 96 dedicated to the structural solver. The wall-clock times and maximum number of CFD mesh nodes achieved by AMR can be seen in Table 7. It is worth noting three outliers in terms of the computational cost: numerical simulation (1) is by far the cheapest due to the use of the coarser CFD mesh, whereas numerical simulations (4) and (8) are

Table 6 Summary of the various critical modeling assumptions considered

Modeling assumption/parameter	Code	Description
CFD mesh resolution	F0	Coarse
	F1	Fine
Forebody dynamics	M0	Fixed
	M1	Free
Canopy material law	C0	Linear, single-scale
	C1	Nonlinear, multiscale
Suspension lines and stiffeners material law	L0	Linear, single-scale
	L1	Nonlinear, multiscale
FSI at suspension lines	S0	Off (uncoupled)
	S1	On (two-way coupled)
Porosity update law	P0	Constant
	P1	Area ratio dependent

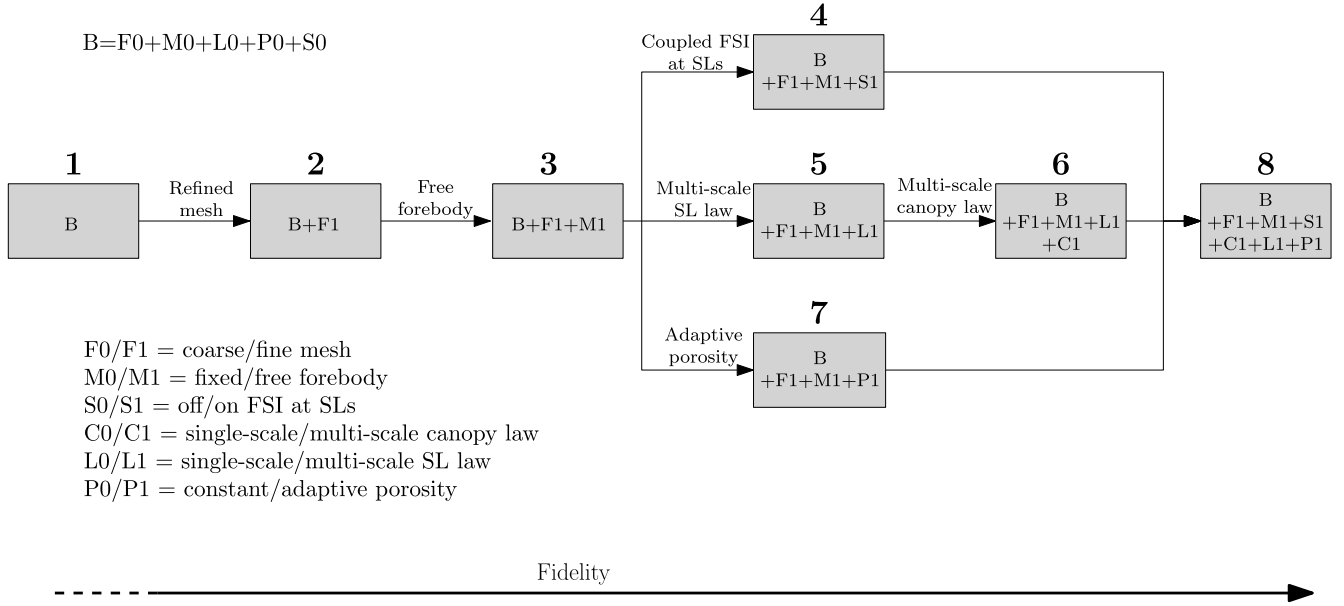


Fig. 7 Strategy for investigating sensitivities with respect to different modeling assumptions.

Table 7 Computational cost and maximum number of CFD nodes for each performed numerical simulation

Numerical simulation	Wall clock time (h)	Maximum number of CFD mesh nodes (millions)
(1)	105	8.3
(2)	180	55.0
(3)	207	54.9
(4)	571	97.4
(5)	181	55.1
(6)	200	49.9
(7)	215	60.2
(8)	638	95.6

substantially more expensive due to the inclusion of the FSI at the suspension lines, which increased the size of the CFD mesh and necessitated a reduction by approximately a factor of 3 of the fluid time step size to avoid nonlinear instability.

1. Dynamic Pressure Time History

In each numerical simulation, the dynamic pressure q_∞ is computed by first evaluating the the free-stream stream velocity vector, in the frame of the forebody, at time t_n , as follows:

$$\mathbf{V}_\infty^n = \mathbf{V}_\infty^0 - \frac{d\mathbf{x}_{CM}}{dt} \bigg|_n \quad (2)$$

where the quantity \mathbf{x}_{CM} denotes the location of the center of mass of the forebody in a frame moving with the forebody at $t = 0$ and the derivative is computed using second-order finite differencing. The dynamic pressure is then computed as $q_\infty^n = (1/2)\rho_\infty \|\mathbf{V}_\infty^n\|^2$, assuming ρ_∞ is constant. The results are shown in Fig. 8 and compared with flight test data.

2. Drag Time History

The parachute force vector \mathbf{F}_p can be represented by two different quantities computed from the outcome of each numerical simulation:

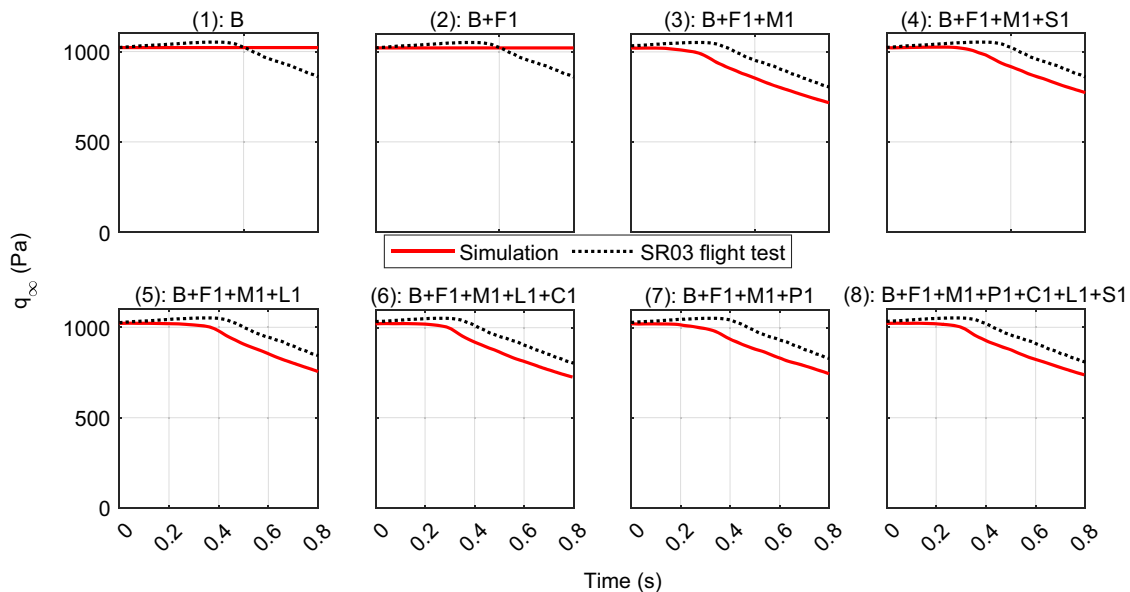


Fig. 8 Comparison of the numerically predicted free-stream dynamic pressure seen by the forebody and counterpart from flight test data (from [6]).

1) The integral of the aerodynamic pressure and viscous forces over the canopy and suspension line embedded surfaces.

2) The sum of the tensions experienced in each of the three triple bridle lines, corrected by the product of the parachute's mass and its acceleration.

The first quantity mentioned previously is the true force generated by the parachute. In contrast, the second quantity is the force imparted by the parachute onto the forebody, which is the one measured during the flight test. This distinction arises from the relative motion between the parachute and the forebody, as well as slack in the suspension lines. Consequently, not all of the force generated by the parachute is transmitted to the forebody. Therefore, an inherent and unavoidable discrepancy between the first quantity and the flight test data is expected, whereas the second quantity is directly comparable to the flight test data. Nonetheless, reporting the first quantity is beneficial as it provides insight into which features of the experimental data are attributable to the aerodynamic properties of the parachute rather than the measurement method.

As for the correction performed in the case of the second quantity described previously, it is due to the deceleration of the system; the parachute force is the difference between the force exerted on it at the load pin attachments and the product of its mass and its acceleration (neglecting gravity). Because of the lack of access to the acceleration of the parachute system—an element not measured in the flight test data—it is assumed that the acceleration of the parachute system is equal to

the acceleration of the forebody for the purpose of calculating this correction. This assumption aligns with the methodology presented in [15]. Explicitly,

$$\mathbf{F}_P = \mathbf{F}_{TB} + m_P \frac{d^2 \mathbf{x}_{CM}}{dt^2} \quad (3)$$

where \mathbf{F}_{TB} is the sum of the tensions in the triple bridle lines (analogous to the load pin measurements) and m_P is the mass of the parachute system (i.e., excluding the forebody). The second derivative with respect to time is computed using second-order finite differencing. The parachute force vector is then projected onto the free-stream direction to compute a representation of the drag. The coefficient of drag is then computed as

$$C_d = \frac{D}{q_\infty S_0} \quad (4)$$

where S_0 is the parachute reference area, computed by summing the as-built areas of the disk, the gap, and the band.

Figures 9 and 10 display the various measures of parachute drag and drag coefficient as functions of time, overlaid with experimental data from [15], which are also computed by correcting the load pin data using the forebody's acceleration. The inclusion of flight test data in Fig. 10 serves only as a reference and is not meant for comparison, as explained by the aforementioned discussion on the

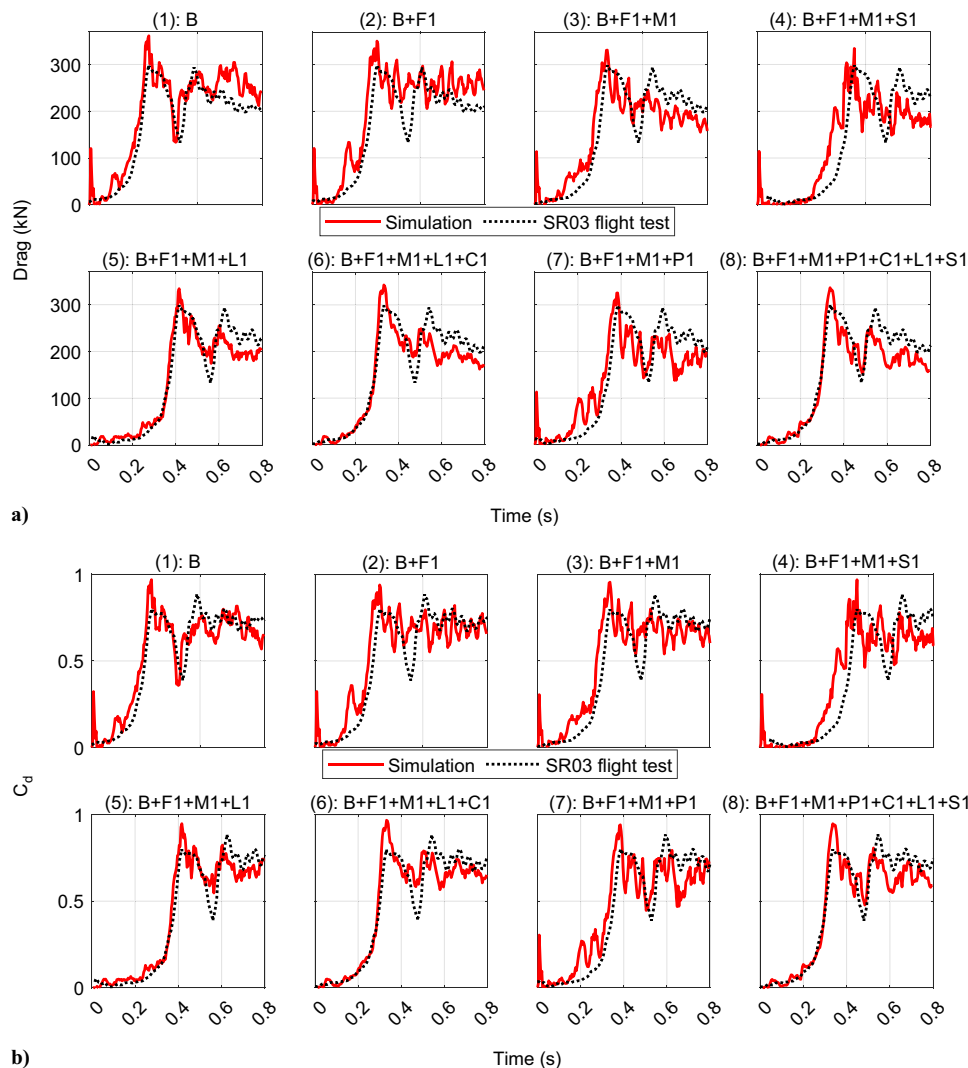


Fig. 9 Comparison of the numerically predicted parachute drag time histories (computed from tension in the triple bridle lines) and load from flight test data (from [15]): a) dimensional and b) nondimensional.

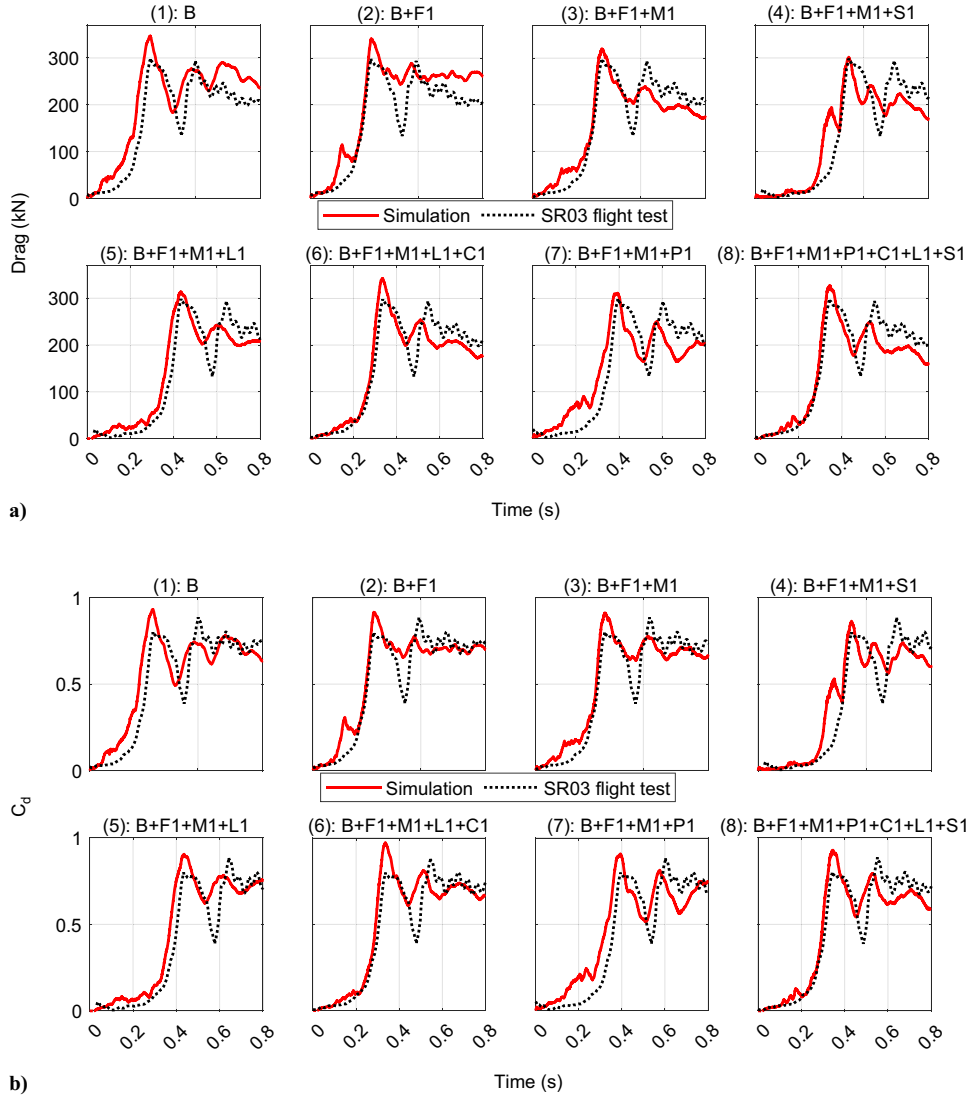


Fig. 10 Comparison of the numerically predicted parachute drag time histories (computed by integrating the aerodynamic forces over the canopy) and load from flight test data (from [15]): a) dimensional and b) nondimensional.

inherent discrepancy between true aerodynamic drag and force experienced by the forebody.

3. Canopy Projected Area

In accordance with the methodology described in [16], the canopy projected area predicted by each numerical simulation is obtained by projecting the canopy onto the plane perpendicular to the forebody axis, computing the convex hull of the corresponding point-cloud, and subsequently computing the area of this hull. Figure 11 presents the canopy projected area as a function of time, overlaid with experimental data obtained from the post-flight image processing in [16].

4. Canopy Skirt Shape

The canopy shape predicted by each numerical simulation is derived by tracking the positions of the nodes located on the leading edge of the band and projecting them onto a plane perpendicular to the forebody axis. Figure 12 shows the canopy skirt shape overlaid with experimental data obtained from post-flight image processing in [16] for three different time instances. It is important to note that the area enclosed by the skirt shape does not represent the projected area referenced in Sec. IV.E.3, as the disk of the parachute, rather than its skirt, can sometimes serve as the boundary of the canopy's projected convex hull.

5. Mach Contours

Figure 13 displays Mach number contours at $t = 0.3$ s simulation time, sliced at the x - z plane in the frame of reference of the forebody, with the parachute system overlaid. Furthermore, Figs. A1–A9 in the Appendix present similar results for different time instances. Note that, in some cases, the parachute deviates sufficiently from the forebody axis, causing it to no longer intersect the Mach contour slice.

F. Discussion

The impact of the various modeling assumptions on the quality of the obtained numerical results can be inferred from the reported QoIs. The accuracy analysis of these results is focused here on the replication of the initial inflation slope, the primary inflation peak, the partial parachute collapse, the secondary inflation peak, the long-term (i.e., postsecondary inflation) behavior, and the general shape of the canopy. It must be noted, however, that there is uncertainty associated with the experimental measurements and an inherent stochastic nature to the parachute deployment, both of which must be considered when interpreting any comparisons with numerical simulation results.

Although numerical simulation (1), which uses a coarser mesh, does relatively well in replicating the drag time history and the partial parachute collapse after the initial inflation peak, clear

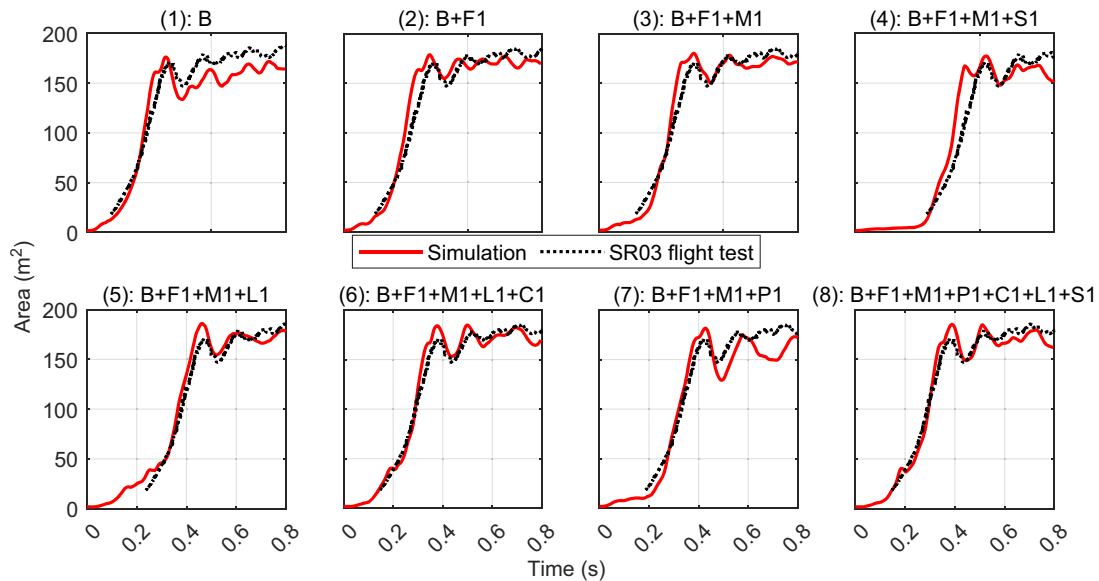


Fig. 11 Comparison of the numerically predicted time histories of the canopy projected area and counterpart from flight test data (from [16]).

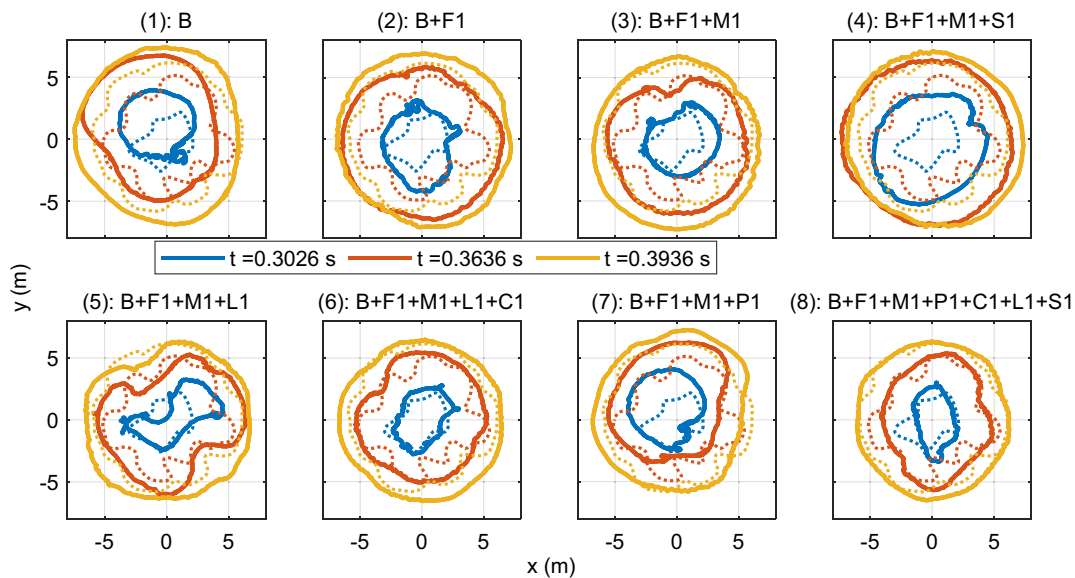


Fig. 12 Comparison of the numerically predicted canopy skirt shapes (solid lines) and counterparts from flight test data (dotted lines, from [16]); the timestamps correspond to the time elapsed since the line-stretch from the experimental data.

qualitative and quantitative changes in the predicted drag time history can be observed in numerical simulation (2) where the CFD mesh is refined. This implies that numerical simulation (1) is a preasymptotic solution with respect to convergence of the CFD discretization. As such, it should not be given much credence; it emphasizes the need for using the finer mesh resolution to obtain reliable and trustworthy numerical predictions. Indeed, it can be seen in Figs. 13 and A2 that the wake unsteadiness predicted by numerical simulation (1) is not yet triggered at the coarser mesh resolution. Additionally, there is a significant underprediction in the canopy projected area when the coarser mesh is used, but not when the finer one is used.

When the forebody is allowed to move freely and is assigned a finite mass, as in numerical simulation (3), two noticeable changes can be seen. First, the inflation peak is lowered and therefore brought closer to its flight test value, which can be attributed to the inertial deceleration effect reducing the tension in the suspension lines. Second, the

post-inflation drag time history is captured more closely, albeit with a slight underprediction (as opposed to the substantial overprediction when the forebody is fixed): this is due to the time-dependent change in the effective free-stream dynamic pressure as the forebody decelerates. In most cases, the underprediction occurs despite a good prediction of the canopy projected area throughout its time history. However, it should be noted that, in all reported numerical simulations, the free-stream density is held at the constant value reported in Table 3. Nonetheless, in the flight test, the parachute system falls through the atmosphere and thus experiences an increase in the free-stream density throughout the inflation. Explicitly, the air density increases by 5% by the time of the second drag peak and by roughly 9% 1 s after the line-stretch phase (approximated from the data plotted in [6]). Moreover, the flight test data exhibit an initial time window in which the dynamic pressure increases as the forebody accelerates, due to the gravity force that exceeds the parachute drag. On the other hand, this is not observed in the numerical simulation data, which indicates a modeling error in

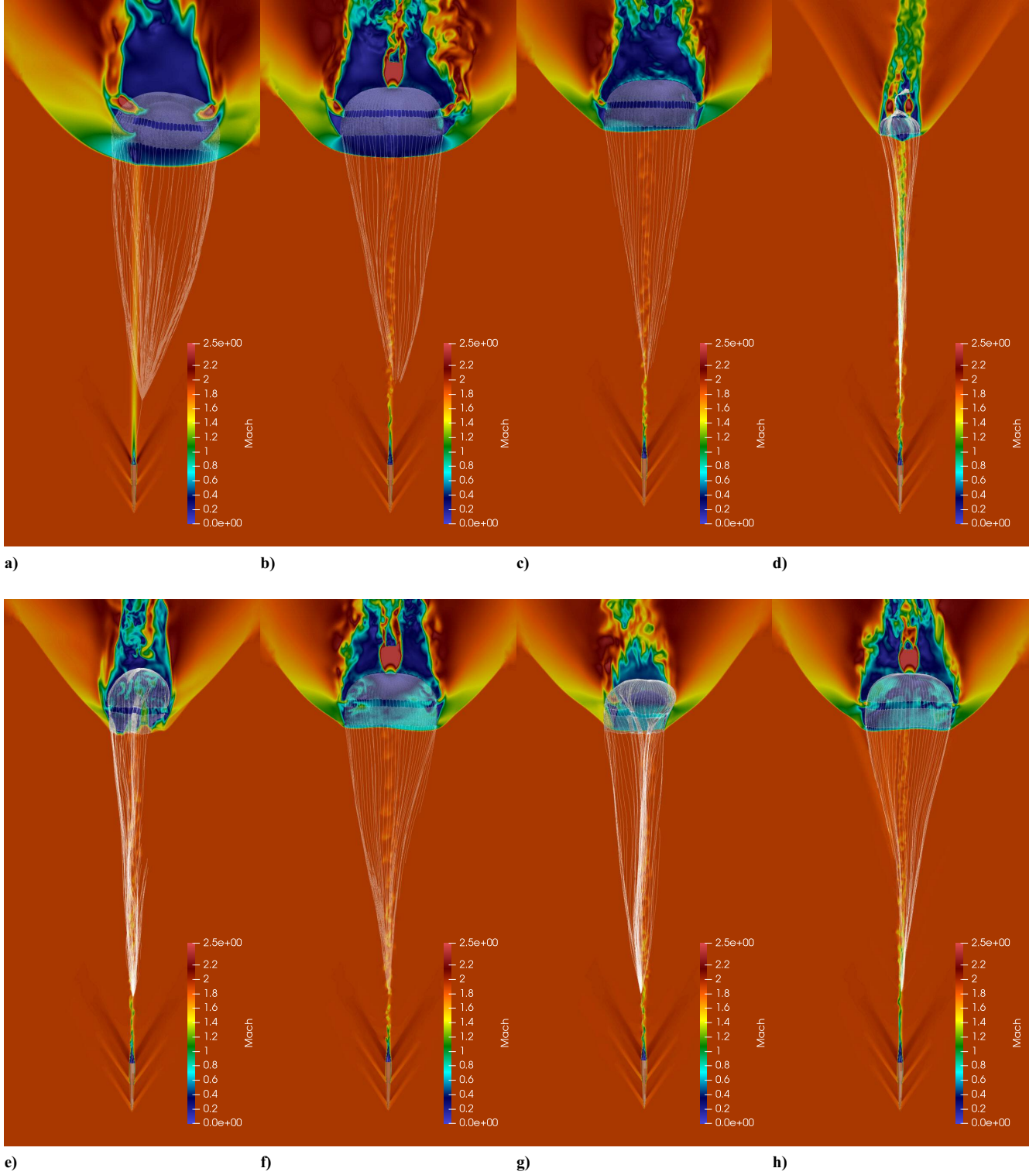


Fig. 13 Snapshots of Mach contours at $t = 0.3$ s predicted by a) numerical simulation (1), b) numerical simulation (2), c) numerical simulation (3), d) numerical simulation (4), e) numerical simulation (5), f) numerical simulation (6), g) numerical simulation (7), and h) numerical simulation (8).

the parachute initial condition. In particular, because the dynamic pressure in the numerical simulations starts decreasing at $t = 0$, the parachute initial shape creates a drag that corresponds to some time after line-stretch, even though the line-stretch free-stream conditions are prescribed at $t = 0$. The absence of this window of acceleration, coupled with inaccuracies in representing the initial condition correctly, can lead to an error in the impulse imparted onto the forebody by the parachute by the time the long-term regime is reached. In Table 8, the integral of the tension in the triple bridle lines with respect to time is

computed from $t = 0$ up until the first and second inflation peaks, which should be equal to the change in momentum of the forebody due to the parachute drag. For the flight test data, the integral is computed from the load pin force measurements from the line-stretch phase until the first and second peaks of the load pin data. It can be seen that, across all but one of the numerical simulations, the impulses computed are larger than those from the flight test data, which means that there is an error in the forebody's momentum by the time the second inflation peak is reached. However, in all but simulations (1) and (2), the

Table 8 Impulse acting on the forebody due to the triple bridle tension (computed as the time integral of the tension) predicted by each performed numerical simulation vs counterpart obtained from flight test data

Numerical simulation	Impulse to first inflation peak, kNs	Impulse to second inflation peak, kNs
(1)	22.37	82.67
(2)	28.05	82.81
(3)	25.97	67.06
(4)	21.73	52.51
(5)	21.48	61.23
(6)	20.92	59.27
(7)	27.54	64.66
(8)	19.92	58.07
Experimental	13.73	54.97

resulting error in the free-stream velocity is less than 1%, and so it is an unlikely source of long-term underprediction. Therefore, neglecting the density increase with time can be identified as the primary contribution to the underprediction of the long-term free-stream dynamic pressure when the forebody is allowed to fall freely. It is worth noting that another potential source of this error is a discrepancy in the angle of attack, which can reduce the portion of the parachute force vector that is projected onto the free-stream direction, which was not investigated here.

If discrete representations of the surfaces of the suspension lines are embedded in the CFD mesh, and thus a two-way coupling is incurred between the CFD solver and FE structural analyzer at the suspension line fluid/structure interfaces, as seen in numerical simulation (4), the reported drag time history changes drastically. Primarily, there is a prolonged initial region of near-zero drag, which is subsequently followed by an intermediate inflation *bump* before the peak inflation is reached. Indeed, it can be seen in Figs. 13 and A4 that the canopy remains in a somewhat tangled state for a large period of time. This is likely caused by the simultaneous impact of the artificially created initial condition and the under-resolution of the suspension lines in the CFD mesh. The narrow accordion-folding initial condition places 80 suspension lines in very close proximity of each other and also places the canopy completely in their wake. Because these tightly packed suspension lines are underresolved, their cylindrical geometries are not captured accurately and their boundary layers are exaggerated. As such, they present a significant source of blockage for the flow downstream of the forebody. Therefore, a large momentum deficit in the flow experienced by the canopy is created, which hinders its ability to inflate. As a result, the canopy initially begins to collapse rather than inflate. Nonetheless, the canopy is eventually able to inflate due to the bending energy stored in the circumferential band beam element at the initial condition, causing the band to immediately flare out and exit the low-speed wake. However, this represents a nonphysical inflation mechanism. The results of this numerical simulation suggest that special care must be taken when attempting to resolve the FSI at the suspension lines, particularly when they are placed in an artificial initial configuration. As noted in [14], the inclusion of FSI at the suspension lines in numerical simulations (4) and (8) slightly aids in capturing the drag trough when the parachute partially collapses. This is hypothesized to result from shock-wake and shock-suspension line interactions. Conversely, it is possible that the influence of FSI at the suspension lines observed in these numerical simulations is nonphysical, stemming from the underresolution of their geometries. However, it is expected that any such effects, whether physical or nonphysical, will be less impactful on the PID during a Mars entry, where the parachute is attached to a blunt capsule rather than the slender ASPIRE forebody.

Across all numerical simulations using single-scale Bernoulli beam elements to represent the braided lines, an initial tangling of the upper part of the disk, near the vent hole, is observed. This is a physically spurious phenomenon caused by the artificially large

bending moment created by the initial condition at the point where the 80 vent lines meet at a tight angle, as seen in Fig. 4: this causes a significant acceleration of the vent lines toward the disk and outwards in the first time step. It also causes the upper part of the canopy to fold onto itself and results in the observed tangling. As has been explained earlier, braided soft ropes have a much lower bending stiffness than their homogeneous counterparts, and therefore such a drastic bending moment should not be present in the parachute system. This effect is manifested in the drag time histories through intermediate bumps in the inflation prior to the initial peak. Moreover, these numerical simulations also exhibit a large spike in the tension near $t = 0$ and generally larger oscillations in the tension measurements, which can be clearly observed in Fig. 9, due to the compressive stiffness of the beam elements. In addition, the canopy skirt exhibits a largely circular shape when the beam elements are used, rather than exhibiting a lobe-like structure, as the bending stiffness of these elements dominates the response of the skirt. These issues are resolved when the multiscale nonlinear bar elements, which exhibit weakness in compression and no bending stiffness, are used to model all suspension lines and stiffeners in the system, as seen in numerical simulation (5). The initial tension spike is no longer present, the intermediate bump during the inflation is suppressed, and the canopy skirt shape is captured more accurately. Furthermore and crucially, the tangling of the parachute near the vent is no longer observed. Overall, this numerical simulation option results in a more physical inflation process and allows for accurate replication of the inflation slope prior to the first drag peak.

The use of the multiscale viscoelastic ANN canopy law, which captures the nonlinearities and time dependence of the fabric response, has a minimal effect on the inflation behavior. Although the dissipation added by the viscoelasticity seems to aid in suppressing spurious oscillations in the early drag time history, it also results in a larger overprediction of the peak drag. This suggests that the ANN material law has a larger compliance relative to the linear material law used, whereas one would expect a fabric material to stiffen in high strain-rate tension. A potential cause for this discrepancy is that the material law was trained at strain rates lower than that experienced in the inflation simulation, causing the strain-rate dependence not to be captured properly and therefore an underprediction of the fabric stiffness in this regime. However, when the viscoelastic ANN material law is used to describe the canopy, the best agreements in both canopy projected area and skirt shape are obtained, which is consistent with the conclusions from [14,30] made in the context of nonlinear elastic ANNs.

It appears from the numerical simulation results that the main impact of using the adaptive porosity is to accentuate the post-inflation partial collapse of the parachute and the breathing oscillations. To explain this, it is first worth noting that it was shown in [16] that the peak drag precedes the peak area by roughly 0.05 s. Because it is expected that the impact of the adaptive porosity should be most prominent at peak area, when the fabric strains are the largest, then it is in accordance that the impact is observed in the drag time history after the first drag peak. Nevertheless, further rigorous work should be performed to establish a mechanism for this phenomenon. It should be noted here again that the nominal porosity value of 0.08 used here is not based on the Heathcoat material used in the SR03 flight test.

Numerical simulation (8) involves using the higher fidelity option for each outlined modeling choice. As such, it has the most accurate overall representation of the drag time history and demonstrates the benefits of each of the higher-fidelity options: the finer mesh resolution for triggering wake unsteadiness, the multiscale suspension line and stiffener material laws for capturing the initial drag slope, the adaptive porosity and suspension line FSI for aiding in capturing the partial parachute collapse, the free forebody dynamics for decreasing the peak drag and long-term parachute drag, and the ANN canopy material law for accurately replicating the projected area and the skirt shape. Still, the overprediction of the peak drag due to the miscalibration of the viscoelastic ANN material

Table 9 Relative error metrics for each numerical simulation's predicted drag, as compared with flight test data

Numerical simulation	$\mathcal{E}_{\text{peak}}, \%$	$\mathcal{E}_{\text{dip}}, \%$	$\mathcal{E}_{\text{pre}}, \%$	$\mathcal{E}_{\text{qs}}, \%$	$\mathcal{E}_{\text{tot}}, \%$
(1)	20.9	0.7	38.4	16.6	18.5
(2)	17.3	55.1	76.8	14.7	22.9
(3)	10.9	30.2	75.5	18.2	23.0
(4)	11.8	33.3	106.8	21.9	31.2
(5)	11.9	32.8	23.2	16.8	16.1
(6)	14.7	41.6	20.6	16.5	16.1
(7)	9.0	9.0	60.8	21.3	26.2
(8)	12.6	16.0	16.4	18.7	16.0

law and the underprediction of the long-term drag due to the underprediction of the post-inflation dynamic pressure need to be addressed to further improve the accuracy and reliability of this high-fidelity numerical simulation.

To provide quantitative support for the previously given discussions, several error metrics of the drag history shown in Fig. 9 have been devised and are summarized in Table 9. They are computed as follows.

1) Peak error:

$$\mathcal{E}_{\text{peak}} = \left| \frac{\max_t D_{\text{exp}}(t) - \max_t D_{\text{sim}}(t)}{\max_t D_{\text{exp}}(t)} \right|$$

2) Dip error:

$$\mathcal{E}_{\text{dip}} = \left| \frac{\min_{t_{i1} < t < t_{i2}} D_{\text{exp}}(t) - \min_{t_{i1} < t < t_{i2}} D_{\text{sim}}(t)}{\min_{t_{i1} < t < t_{i2}} D_{\text{exp}}(t)} \right|$$

3) Pre-inflation integrated error:

$$\mathcal{E}_{\text{pre}} = \frac{\int_0^{t_{i1}} |D_{\text{exp}}(t) - D_{\text{sim}}(t)| dt}{\int_0^{t_{i1}} |D_{\text{exp}}(t)| dt}$$

4) Quasi-steady integrated error:

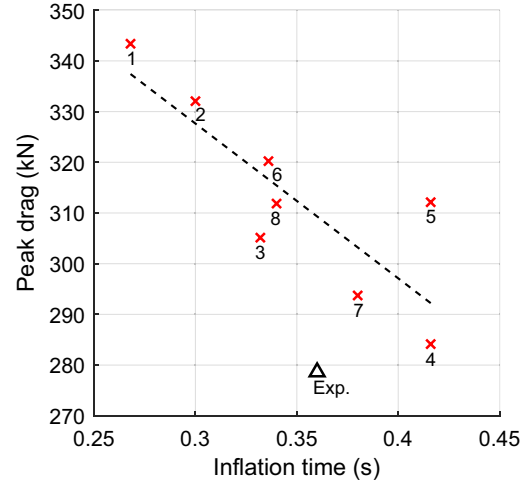
$$\mathcal{E}_{\text{qs}} = \frac{\int_{t_{i2}}^{T_f} |D_{\text{exp}}(t) - D_{\text{sim}}(t)| dt}{\int_{t_{i2}}^{T_f} |D_{\text{exp}}(t)| dt}$$

5) Total integrated error:

$$\mathcal{E}_{\text{tot}} = \frac{\int_0^{T_f} |D_{\text{exp}}(t) - D_{\text{sim}}(t)| dt}{\int_0^{T_f} |D_{\text{exp}}(t)| dt}$$

where $D_{\text{exp}}(t)$ represents the (time-shifted) experimental drag data, $D_{\text{sim}}(t)$ represents the numerical simulation drag data, T_f is the maximum numerical simulation time, t_{i1} is the time of the first inflation peak, and t_{i2} is the time of the second inflation peak.

Interestingly, the eight reported numerical simulations exhibit appreciable variances in both the inflation times and peak drags. The variability of the inflation times is not entirely surprising, given that an artificial initial condition that can cause the initial prediction of nonphysical and somewhat arbitrary states was used. However, one would expect the impact of this initial behavior to diminish by the time the parachute inflates. Nevertheless, a clear inverse correlation can be observed between the inflation time and the peak drag, as shown in Fig. 14. Fundamentally, this suggests a strong sensitivity of the predicted peak drag, which is a critical QoI in parachute design, to the initial inflation behavior and highlights the importance of the initial condition. A potential explanation for the

**Fig. 14** Correlation of inflation time with peak drag (computed from the triple bridle tension data) for each performed numerical simulation and for the flight test data.

observed correlation is that, when the inflation occurs more quickly, the canopy has more momentum, which allows it to overshoot the peak area. Another possible explanation is that the faster inflation does not allow for enough time for mass to expel from the vent hole and gaps, thus leading to a larger build-up of pressure in the canopy.

V. Conclusions

This paper presents a thorough study of the performance of a computational framework for the numerical simulation of supersonic parachute inflation dynamics, through its validation and sensitivity analysis with respect to modeling assumptions and parameters. The framework is implemented in AERO Suite—a software suite for the numerical simulation of highly nonlinear FSI problems. The validation is performed both quantitatively, through the comparison of key quantities of interest and counterparts obtained from the ASPIRE SR03 flight test data, and qualitatively, through a discussion of the trends and observed physical phenomena. Overall, all numerical simulations performed using the computational framework and different levels of fidelity deliver results that are in reasonably good agreement with the flight test data, with an edge for those featuring the higher fidelity modeling options. Specifically, it is found that a finer CFD mesh resolution is necessary (as can be expected) to resolve the relevant flow features, the free dynamics of the forebody are needed to capture more accurately the long-term behavior of the drag and the inflation peak, modeling the FSI at the suspension lines and the adaptive porosity of the fabric slightly assist in resolving the post-inflation partial collapse, the multiscale material modeling of the suspension lines and stiffeners drastically improves the prediction of the early inflation behavior, and the multiscale material modeling of the canopy results in a better replication of the time history of the canopy shape. However, the modeling of the FSI at the suspension lines incurs a large increase in the computational burden while having a relatively small impact on the results; thus, its worth should be investigated further. Despite the overall agreements between the numerical results and their counterparts obtained from flight test data, the numerical simulations are found to underestimate the long-term behavior of the drag and overestimate its peak value. As such, future work should revisit the data-driven modeling of the viscoelastic material of the canopy using an artificial neural network by training it at higher strain-rates, akin to those experienced during the online numerical simulations, exploit the atmospheric model readily available in AERO Suite to account for the increase in the free-stream density during a numerical simulation, and revisit the parachute configuration chosen for defining the initial condition of the supersonic PID problem.

Appendix

Figures A1–A8 in this appendix present Mach contours overlaid with the parachute structural system for each numerical simulation, taken at four different time instances. The Mach contours are

derived as slices at the x – z plane in the frame of reference of the forebody. Note that, in some cases, the parachute deviates sufficiently from the forebody axis such that it no longer intersects the Mach contour slice.

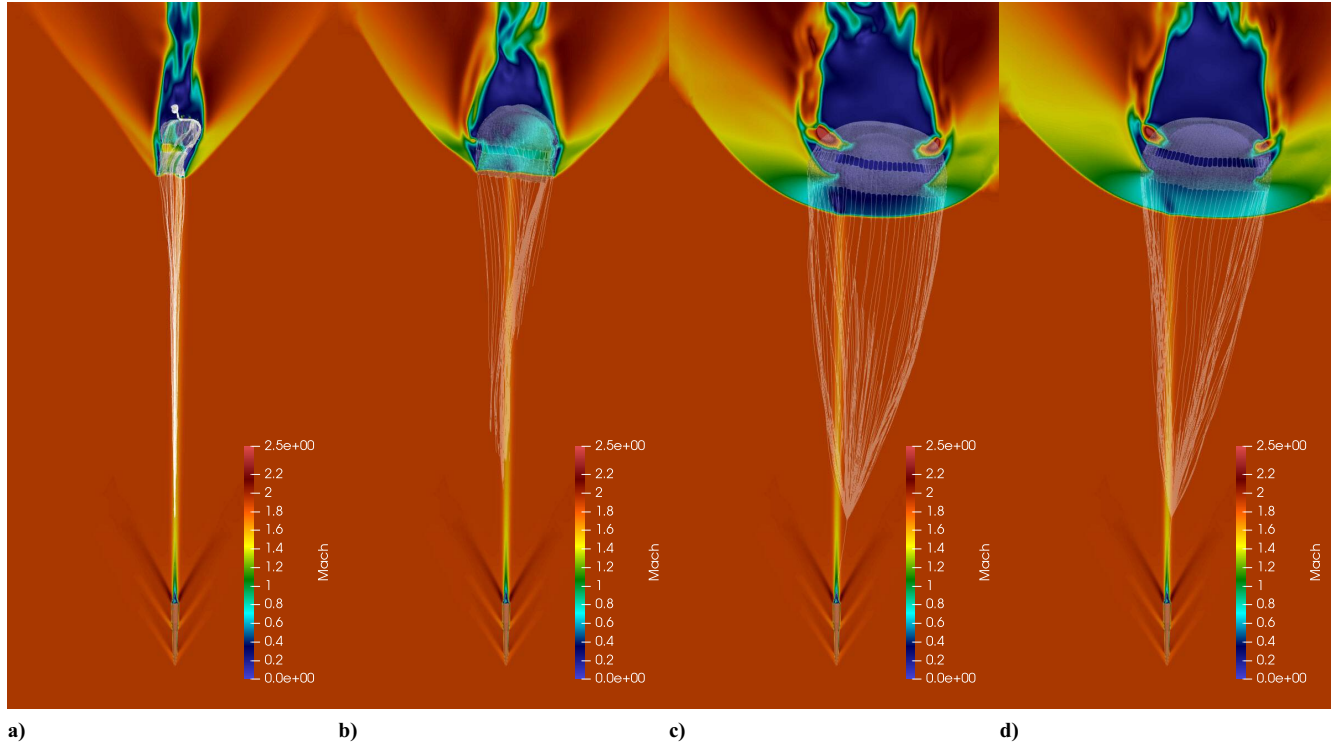


Fig. A1 Snapshots of Mach contours predicted by numerical simulation (1): a) $t = 0.1$ s, b) $t = 0.2$ s, c) $t = 0.3$ s, and d) $t = 0.5$ s.

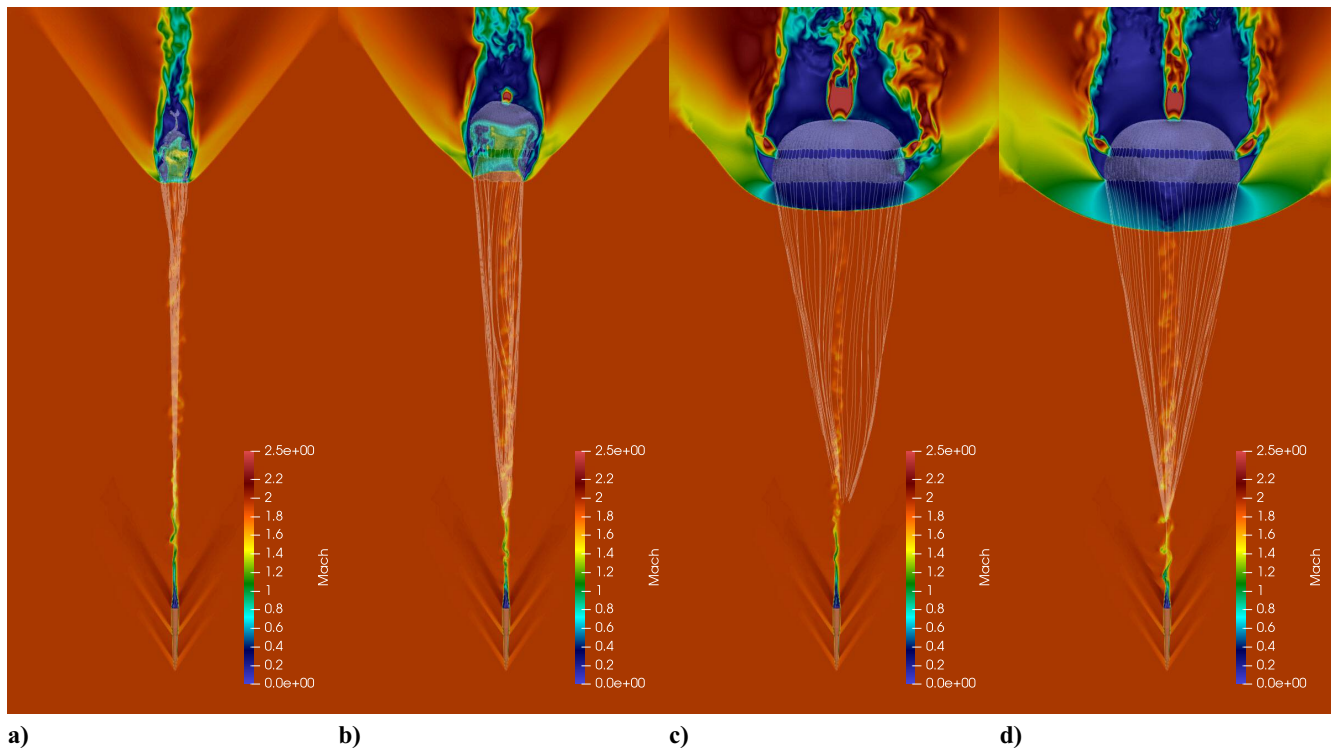


Fig. A2 Snapshots of Mach contours predicted by numerical simulation (2): a) $t = 0.1$ s, b) $t = 0.2$ s, c) $t = 0.3$ s, and d) $t = 0.5$ s.

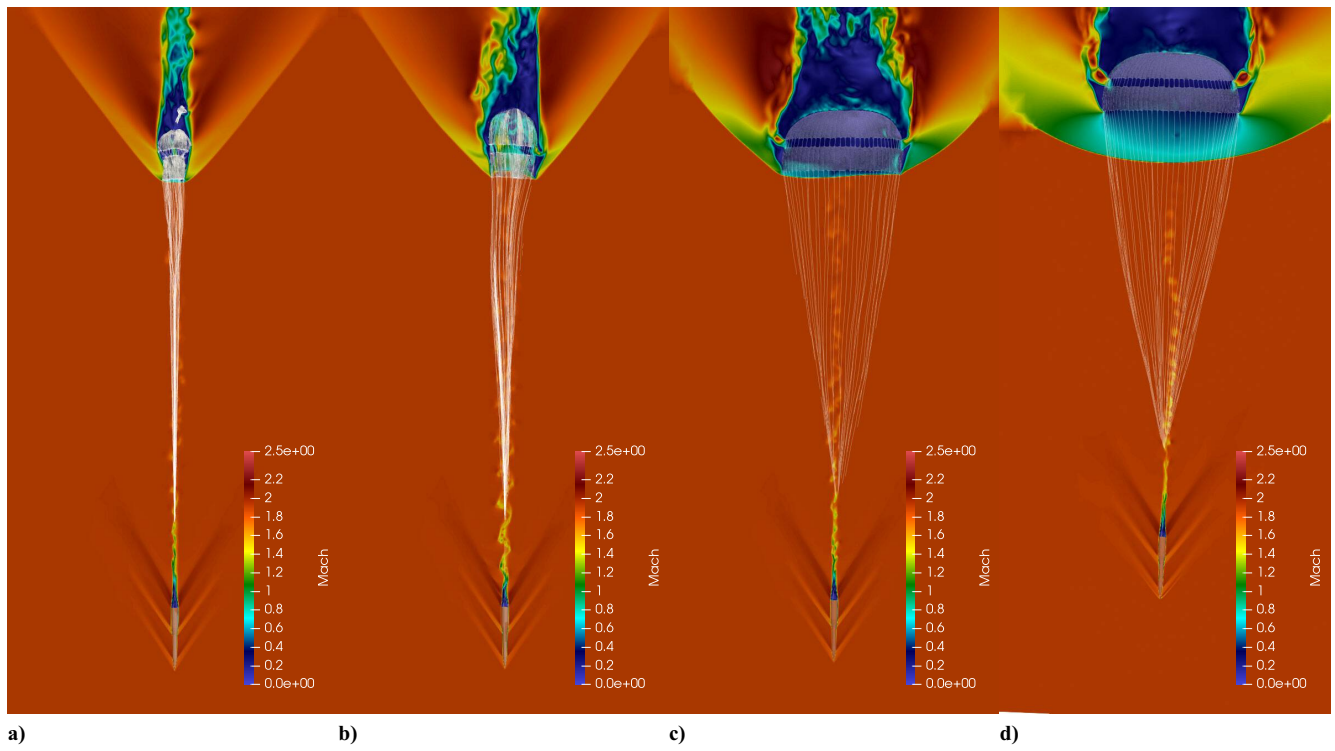


Fig. A3 Snapshots of Mach contours predicted by numerical simulation (3): a) $t = 0.1$ s, b) $t = 0.2$ s, c) $t = 0.3$ s, and d) $t = 0.5$ s.

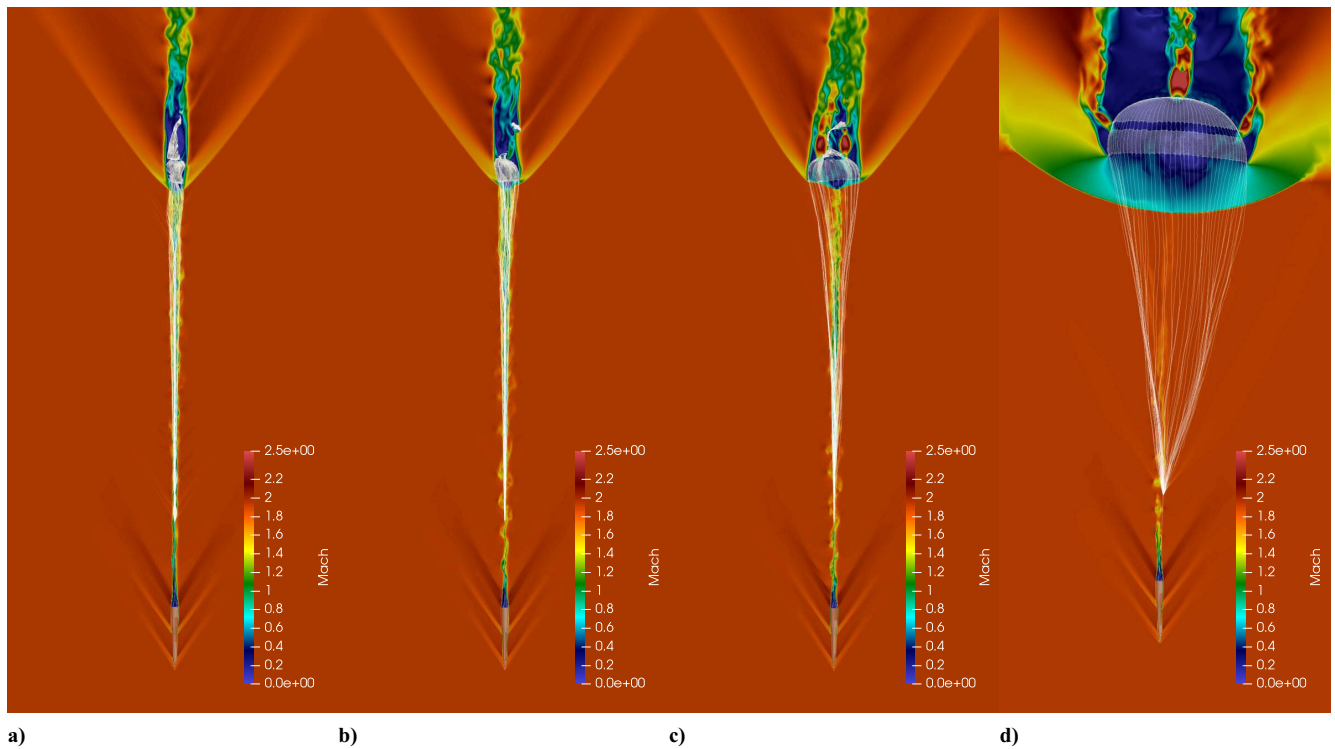


Fig. A4 Snapshots of Mach contours predicted by numerical simulation (4): a) $t = 0.1$ s, b) $t = 0.2$ s, c) $t = 0.3$ s, and d) $t = 0.5$ s.

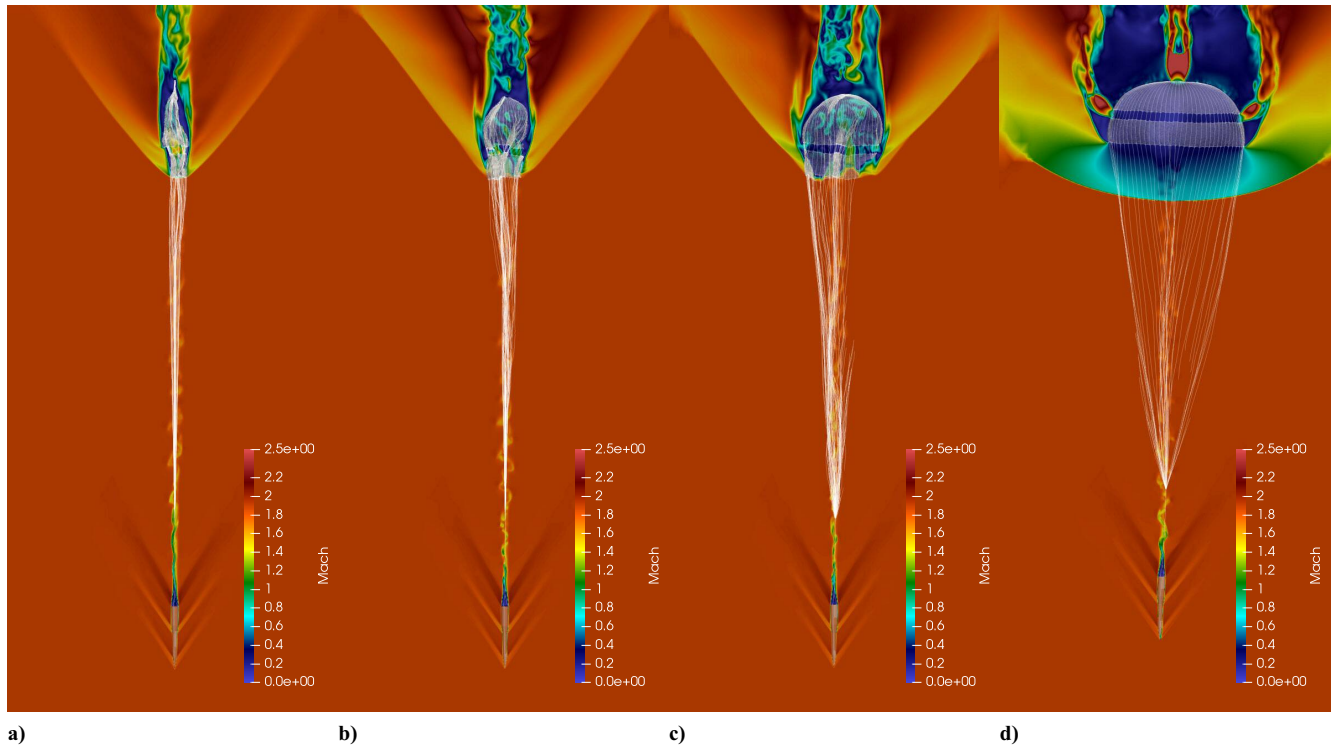


Fig. A5 Snapshots of Mach contours predicted by numerical simulation (5): a) $t = 0.1$ s, b) $t = 0.2$ s, c) $t = 0.3$ s, and d) $t = 0.5$ s.

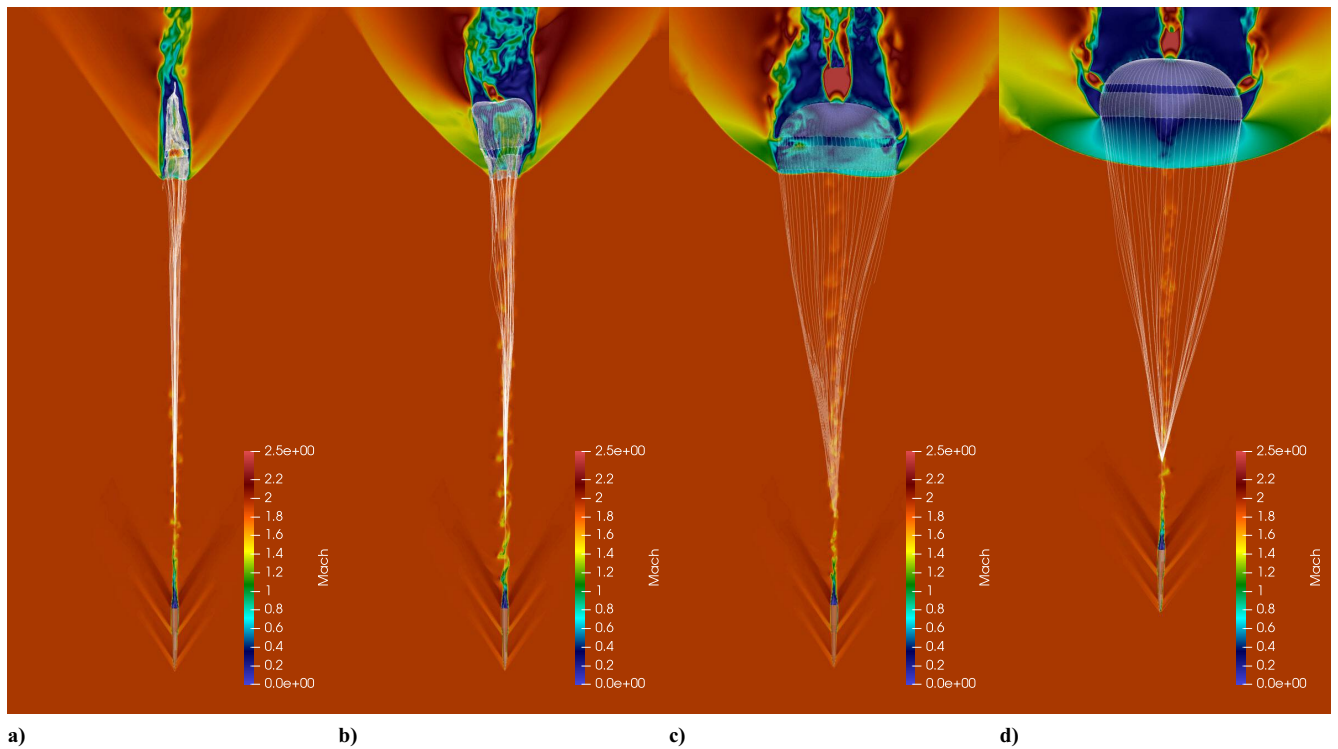


Fig. A6 Snapshots of Mach contours predicted by numerical simulation (6): a) $t = 0.1$ s, b) $t = 0.2$ s, c) $t = 0.3$ s, and d) $t = 0.5$ s.

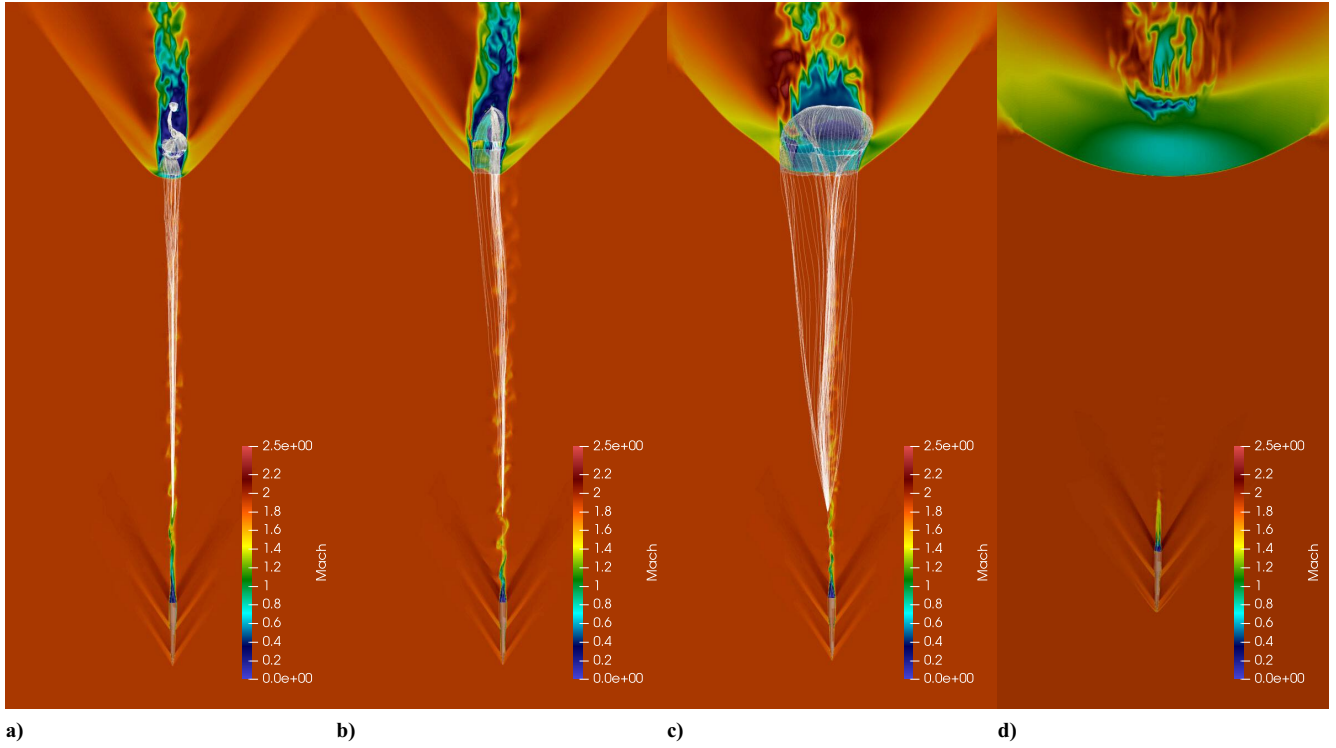


Fig. A7 Snapshots of Mach contours predicted by numerical simulation (7): a) $t = 0.1$ s, b) $t = 0.2$ s, c) $t = 0.3$ s, and d) $t = 0.5$ s.

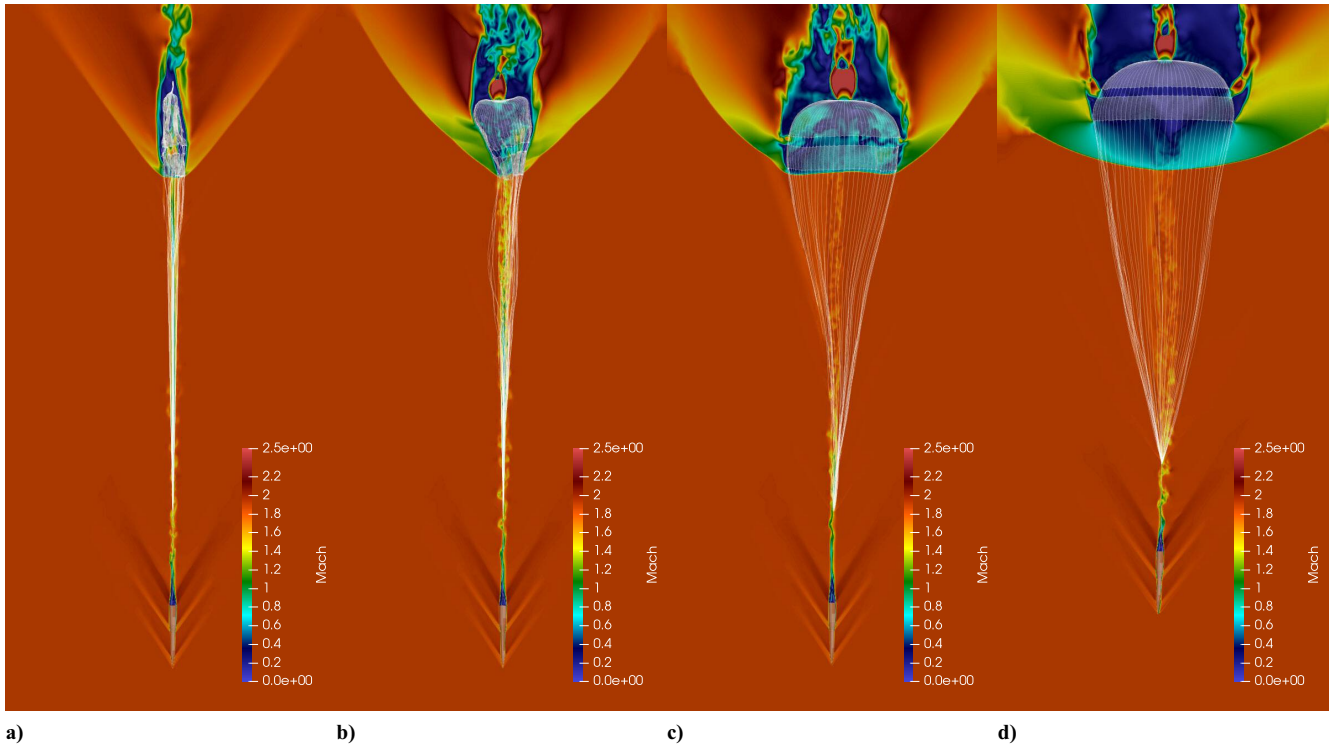


Fig. A8 Snapshots of Mach contours predicted by numerical simulation (8): a) $t = 0.1$ s, b) $t = 0.2$ s, c) $t = 0.3$ s, and d) $t = 0.5$ s.

Acknowledgments

Faisal As'ad, Philip Avery, and Charbel Farhat acknowledge partial support by the National Aeronautics and Space Administration (NASA) under Early Stage Innovations (ESI) Grant 80NSSC 21K0228 and partial support by the Jet Propulsion Laboratory (JPL) under Award RSA No. 1670712. Parts of this research were carried out at the Jet Propulsion Laboratory, California Institute of Technology, under a contract with the National Aeronautics and Space Administration funded through the Strategic University Research Partnership (SURP) program.

References

- [1] Takizawa, K., and Tezduyar, T., "Computational Methods for Parachute Fluid-Structure Interactions," *Archives of Computational Methods in Engineering*, Vol. 19, March 2012, pp. 125–169.
<https://doi.org/10.1007/s11831-012-9070-4>
- [2] Karazis, K., Kamakoti, R., Cirak, F., and Pantano, C., "A Computational Study of Supersonic Disk-Gap-Band Parachutes Using Large-Eddy Simulation Coupled to a Structural Membrane," *Journal of Fluids and Structures*, Vol. 27, No. 2, Feb. 2011, pp. 175–192.
<https://doi.org/10.1016/j.jfluidstructs.2010.11.007>
- [3] Lingard, J., and Darley, M., "Simulation of Parachute Fluid Structure Interaction in Supersonic Flow," *18th AIAA Aerodynamic Decelerator Systems Technology Conference and Seminar*, AIAA Paper 2005-1607, 2005.
<https://doi.org/10.2514/6.2005-1607>
- [4] Barnhardt, M., Drayna, T., Nompelis, I., Candler, G., and Garrard, W., "Detached Eddy Simulations of the MSL Parachute at Supersonic Conditions," *19th AIAA Aerodynamic Decelerator Systems Technology Conference and Seminar*, AIAA Paper 2007-2529, 2007.
<https://doi.org/10.2514/6.2007-2529>
- [5] Muppidi, S., O'Farrell, C., Tanner, C., Van Norman, J. W., and Clark, I. G., "Modeling and Flight Performance of Supersonic Disk-Gap-Band Parachutes in Slender Body Wakes," *2018 Atmospheric Flight Mechanics Conference*, AIAA Paper 2018-3623, 2018.
<https://doi.org/10.2514/6.2018-3623>
- [6] O'Farrell, C., Sonneveldt, B. S., Karhgaard, C., Tynis, J. A., and Clark, I. G., "Overview of the ASPIRE Project's Supersonic Flight Tests of a Strengthened DGB Parachute," *2019 IEEE Aerospace Conference*, IEEE, New York, 2019, pp. 1–18.
<https://doi.org/10.1109/AERO.2019.8741611>
- [7] Clark, I. G., Gallon, J. C., and Witkowski, A., "Parachute Decelerator System Performance During the Low Density Supersonic Decelerator Program's First Supersonic Flight Dynamics Test," *23rd AIAA Aerodynamic Decelerator Systems Technology Conference*, AIAA Paper 2015-2130, 2015.
<https://doi.org/10.2514/6.2015-2130>
- [8] O'Farrell, C., Brandeau, E. J., Tanner, C., Gallon, J. C., Muppidi, S., and Clark, I. G., "Reconstructed Parachute System Performance During the Second LDSD Supersonic Flight Dynamics Test," *AIAA Atmospheric Flight Mechanics Conference*, AIAA Paper 2016-3242, 2016.
<https://doi.org/10.2514/6.2016-3242>
- [9] Huang, D. Z., Avery, P., Farhat, C., Rabinovitch, J., Derkevorkian, A., and Peterson, L. D., "Modeling, Simulation and Validation of Supersonic Parachute Inflation Dynamics During Mars Landing," *AIAA Scitech 2020 Forum*, AIAA Paper 2020-0313, 2020.
<https://doi.org/10.2514/6.2020-0313>
- [10] Xue, Y., Li, Y., Min, L., and Haoifei, P., "Fluid Structure Interaction Simulation of Supersonic Parachute Inflation by an Interface Tracking Method," *Chinese Journal of Aeronautics*, Vol. 33, No. 6, 2020, pp. 1692–1702.
<https://doi.org/10.1016/j.cja.2020.03.005>
- [11] Cadieux, F., and Barad, M. F., "Fluid-Structure Interaction Simulations of Supersonic Parachute Inflation: Model Sensitivities," *AIAA Aviation Forum and Ascend 2024*, AIAA Paper 2024-4225, 2024.
<https://doi.org/10.2514/6.2024-4225>
- [12] Farhat, C., Geuzaine, P., and Brown, G., "Application of a Three-Field Nonlinear Fluid-Structure Formulation to the Prediction of the Aeroelastic Parameters of an F-16 Fighter," *Computers & Fluids*, Vol. 32, No. 1, 2003, pp. 3–29.
[https://doi.org/10.1016/S0045-7930\(01\)00104-9](https://doi.org/10.1016/S0045-7930(01)00104-9)
- [13] Geuzaine, P., Brown, G., Harris, C., and Farhat, C., "Aeroelastic Dynamic Analysis of a Full F-16 Configuration for Various Flight Conditions," *AIAA Journal*, Vol. 41, No. 3, 2003, pp. 363–371.
<https://doi.org/10.2514/2.1975>
- [14] As'ad, F., Avery, P., Farhat, C., Rabinovitch, J., and Lobbia, M., "Validation of a High-Fidelity Supersonic Parachute Inflation Dynamics Model and Best Practice," *AIAA Scitech 2022 Forum*, AIAA Paper 2022-0351, 2022.
<https://doi.org/10.2514/6.2022-0351>
- [15] Muppidi, S., O'Farrell, C., Van Norman, J. W., and Clark, I. G., "ASPIRE Aerodynamic Models and Flight Performance," *AIAA Aviation 2019 Forum*, AIAA Paper 2019-3376, 2019.
<https://doi.org/10.2514/6.2019-3376>
- [16] Rabinovitch, J., Griffin, G. S., Seto, W., O'Farrell, C., Tanner, C. L., and Clark, I. G., "Full-Scale Supersonic Parachute Shape Reconstruction Using Three-Dimensional Stereo Imagery," *Journal of Spacecraft and Rockets*, Vol. 57, No. 6, 2020, pp. 1139–1152.
<https://doi.org/10.2514/1.A34717>
- [17] Rabinovitch, J., As'ad, F., Avery, P., Farhat, C., Ataei, N., and Lobbia, M., "Update: Modeling Supersonic Parachute Inflation for Mars Spacecraft," *26th AIAA Aerodynamic Decelerator Systems Technology Conference*, AIAA Paper 2022-2746, 2022.
<https://doi.org/10.2514/6.2022-2746>
- [18] Sonneveldt, B. S., Clark, I. G., and O'Farrell, C., "Summary of the Advanced Supersonic Parachute Inflation Research Experiments (ASPIRE) Sounding Rocket Tests with a Disk-Gap-Band Parachute," *AIAA Aviation 2019 Forum*, AIAA Paper 2019-3482, 2019.
<https://doi.org/10.2514/6.2019-3482>
- [19] Tutt, B. A., Lowry, C. W., Clark, I. G., and Tanner, C., "Design Overview of the Strengthened Mars 2020 Parachute Assembly," *AIAA Aviation 2019 Forum*, AIAA Paper 2019-3479, 2019.
<https://doi.org/10.2514/6.2019-3479>
- [20] Cruz, J. R., Hennings, E., and Runnells, P., "Permeability of a New Parachute Fabric—Measurements, Modeling, and Application," NASA TR 20190001214, 2018.
- [21] Hinada, M., Inatani, Y., Nakajima, T., and Honda, M., "Parachute Deployment Experiment in Transonic and Supersonic Wind Tunnels," *11th Aerodynamic Decelerator Systems Technology Conference*, AIAA Paper 1997-0859, 1991.
<https://doi.org/10.2514/6.1991-859>
- [22] Farhat, C., Gerbeau, J.-F., and Rallu, A., "FIVER: A Finite Volume Method Based on Exact Two-Phase Riemann Problems and Sparse Grids for Multi-Material Flows with Large Density Jumps," *Journal of Computational Physics*, Vol. 231, No. 19, Aug. 2012, pp. 6360–6379.
<https://doi.org/10.1016/j.jcp.2012.05.026>
- [23] Farhat, C., and Lakshminarayan, V. K., "An ALE Formulation of Embedded Boundary Methods for Tracking Boundary Layers in Turbulent Fluid-Structure Interaction Problems," *Journal of Computational Physics*, Vol. 263, April 2014, pp. 53–70.
<https://doi.org/10.1016/j.jcp.2014.01.018>
- [24] Ren, Y.-X., "A Robust Shock-Capturing Scheme Based on Rotated Riemann Solvers," *Computers & Fluids*, Vol. 32, No. 10, 2003, pp. 1379–1403.
[https://doi.org/10.1016/S0045-7930\(02\)00114-7](https://doi.org/10.1016/S0045-7930(02)00114-7)
- [25] Farhat, C., Geuzaine, P., and Grandmont, C., "The Discrete Geometric Conservation Law and the Nonlinear Stability of ALE Schemes for the Solution of Flow Problems on Moving Grids," *Journal of Computational Physics*, Vol. 174, No. 2, 2001, pp. 669–694.
<https://doi.org/10.1006/jcph.2001.6932>
- [26] Borker, R., Huang, D., Grimberg, S., Farhat, C., Avery, P., and Rabinovitch, J., "Mesh Adaptation Framework for Embedded Boundary Methods for Computational Fluid Dynamics and Fluid-Structure Interaction," *International Journal for Numerical Methods in Fluids*, Vol. 90, No. 8, 2019, pp. 389–424.
<https://doi.org/10.1002/fld.4728>
- [27] Karypis, G., Schloegel, K., Kumar, V., and METIS, P., "Parallel Graph Partitioning and Sparse Matrix Ordering Library," University of Minnesota, 1998.
- [28] Farhat, C., Rallu, A., Wang, K., and Belytschko, T., "Robust and Provably Second-Order Explicit-Explicit and Implicit-Explicit Staggered Time-Integrators for Highly Nonlinear Fluid-Structure Interaction Problems," *International Journal for Numerical Methods in Engineering*, Vol. 84, No. 1, Aug. 2010, pp. 73–107.
<https://doi.org/10.1002/nme.2883>
- [29] As'ad, F., and Farhat, C., "A Mechanics-Informed Deep Learning Framework for Data-Driven Nonlinear Viscoelasticity," *Computer Methods in Applied Mechanics and Engineering*, Vol. 417, Part A, Dec. 2023, Paper 116463.
<https://doi.org/10.1016/j.cma.2023.116463>
- [30] As'ad, F., Avery, P., and Farhat, C., "A Mechanics-Informed Artificial Neural Network Approach in Data-Driven Constitutive Modeling," *International Journal for Numerical Methods in Engineering*, Vol. 123,

- No. 12, 2022, pp. 2738–2759.
<https://doi.org/10.1002/nme.6957>
- [31] Derkevorkian, A., Avery, P., Farhat, C., Rabinovitch, J., and Peterson, L., “Effects of Structural Parameters on the FSI Simulation of Supersonic Parachute Deployments,” *AIAA Aviation 2019 Forum*, AIAA Paper 2019-3276, 2019.
<https://doi.org/10.2514/6.2019-3276>
- [32] Amirkhizi, A., Blanas, M., Campos, F., Krantz, K., Drane, P., Sherwood, J., and Witkowski, A., “Material Characteristics of F-111 (PIA-C-44378) Canopy Fabric in Uniaxial and Biaxial Conditions,” *26th AIAA Aerodynamic Decelerator Systems Technology Conference*, AIAA Paper 2022-2724, 2022.
<https://doi.org/10.2514/6.2022-2724>
- [33] Brown, K., Glass, M., Summers, R., Heinsteins, M., Gullerud, A., et al., “Algorithms for Contact in a Multiphysics Environment,” Sandia National Lab. TR SAND2004-5486, 2001.
- [34] Maman, N., and Farhat, C., “Matching Fluid and Structure Meshes for Aeroelastic Computations: A Parallel Approach,” *Computers & Structures*, Vol. 54, No. 4, 1995, pp. 779–785.
[https://doi.org/10.1016/0045-7949\(94\)00359-B](https://doi.org/10.1016/0045-7949(94)00359-B)
- [35] Huang, D. Z., Wong, M. L., Lele, S. K., and Farhat, C., “Homogenized Flux-Body Force Treatment of Compressible Viscous Porous Wall Boundary Conditions,” *AIAA Journal*, Vol. 59, No. 6, 2021, pp. 2045–2059.
<https://doi.org/10.2514/1.J059945>
- [36] Phillippe, C., Mattei, M., Panerai, F., and Villafañe Roca, L., “In-Situ Micro-Scale Characterization of Parachute Textiles with Micro-Tomography and Machine Learning,” *AIAA Scitech 2023 Forum*, AIAA Paper 2023-0141, 2023.
<https://doi.org/10.2514/6.2023-0141>
- [37] Ghasimi, S. D., Rabinovitch, J., Chacon, L., Poovathingal, S. J., Phillippe, C. A., Foster, C., Mattei, M., Roca, L. V., Panerai, F., As'ad, F., Avery, P., Farhat, C., Lobbia, M., and Ataei, N., “Permeability Modeling of Mars Parachute Broadcloth Materials,” *AIAA Aviation 2024 Forum*, AIAA Paper 2024-4224, 2024.
<https://doi.org/10.2514/6.2024-4224>
- [38] O'Farrell, C., Siegel, K. J., Navarro, C., and Lowry, C., “Permeability of the Sample Retrieval Lander's Candidate Parachute Fabric,” *AIAA Aviation Forum and Ascend 2024*, AIAA Paper 2024-4223, 2024.
<https://doi.org/10.2514/6.2024-4223>
- [39] Reichardt, H., “Vollständige Darstellung der Turbulenten Geschwindigkeitsverteilung in Glatten Leitungen,” *ZAMM-Journal of Applied Mathematics and Mechanics/Zeitschrift für Angewandte Mathematik und Mechanik*, Vol. 31, No. 7, 1951, pp. 208–219.
<https://doi.org/10.1002/zamm.19510310704>
- [40] Vreman, A. W., “An Eddy-Viscosity Subgrid-Scale Model for Turbulent Shear Flow: Algebraic Theory and Applications,” *Physics of Fluids*, Vol. 16, No. 10, 2004, pp. 3670–3681.
<https://doi.org/10.1063/1.1785131>
- [41] Huang, D. Z., Avery, P., and Farhat, C., “An Embedded Boundary Approach for Resolving the Contribution of Cable Subsystems to Fully Coupled Fluid-Structure Interaction,” *International Journal for Numerical Methods in Engineering*, Vol. 122, No. 19, 2021, pp. 5409–5429.
<https://doi.org/10.1002/nme.6322>
- [42] Venkatakrishnan, V., “Convergence to Steady State Solutions of the Euler Equations on Unstructured Grids with Limiters,” *Journal of Computational Physics*, Vol. 118, No. 1, 1995, pp. 120–130.
<https://doi.org/10.1006/jcph.1995.1084>
- [43] Xue, X., Koyama, H., and Nakamura, Y., “Numerical Simulation of Supersonic Aerodynamic Interaction of a Parachute System,” *Transactions of the Japan Society for Aeronautical and Space Sciences, Aerospace Technology Japan*, Vol. 11, May 2013, pp. 33–42.
<https://doi.org/10.2322/tastj.11.33>
- [44] Shunchen, N., Li, Y., Yanjun, L., Zhihong, S., and Bowen, Q., “Fluid Structure Interaction of Supersonic Parachute with Material Failure,” *Chinese Journal of Aeronautics*, Vol. 36, No. 10, 2023, pp. 90–100.
<https://doi.org/10.1016/j.cja.2023.06.026>
- [45] Kou, Z., and Zhan, H., “Effects of Forebody on Supersonic Parachute Aerodynamic Performance,” *Journal of Physics: Conference Series*, Vol. 2228, No. 1, 2022, Paper 012013.
<https://doi.org/10.1088/1742-6596/2228/1/012013>
- [46] Xue, X.-P., Koyama, H., Nakamura, Y., and Wen, C.-Y., “Effects of Suspension Line on Flow Field Around a Supersonic Parachute,” *Aerospace Science and Technology*, Vol. 43, June 2015, pp. 63–70.
<https://doi.org/10.1016/j.ast.2015.02.014>
- [47] Heinrich, H. G., and Haak, E. L., “Stability and Drag of Parachutes with Varying Effective Porosity,” Univ. of Minnesota AFFDL-TR-71, 1971.
- [48] Payne, P. R., “The Theory of Fabric Porosity as Applied to Parachutes in Incompressible Flow,” *Aeronautical Quarterly*, Vol. 29, No. 3, 1978, pp. 175–206.
<https://doi.org/10.1017/S000192590000843X>

R. Ohayon
Associate Editor